

ORCA - Online Research @ Cardiff

This is an Open Access document downloaded from ORCA, Cardiff University's institutional repository:https://orca.cardiff.ac.uk/id/eprint/181738/

This is the author's version of a work that was submitted to / accepted for publication.

Citation for final published version:

Hinchey, A.M., Hinchey, J.G., Sandeman, H.A., Lissenberg, C.J., Rayner, N. and Marin, D. M. 2025. Silurian mafic magmatism related to post-collisional extension, Appalachian orogen, western Newfoundland. Canadian Journal of Earth Sciences

Publishers page:

Please note:

Changes made as a result of publishing processes such as copy-editing, formatting and page numbers may not be reflected in this version. For the definitive version of this publication, please refer to the published source. You are advised to consult the publisher's version if you wish to cite this paper.

This version is being made available in accordance with publisher policies. See http://orca.cf.ac.uk/policies.html for usage policies. Copyright and moral rights for publications made available in ORCA are retained by the copyright holders.



Silurian mafic magmatism related to post-collisional extension, Appalachian orogen, western Newfoundland A.M. Hinchey^{1*}, J.G. Hinchey¹, H.A. Sandeman¹, C.J. Lissenberg², N. Rayner³ and Daniela Mendoza Marin¹ ¹Geological Survey, Department of Industry, Energy and Technology, Government of Newfoundland and Labrador, P.O. Box 8700, St. John's, NL A1B 4J6. ² School of Earth and Environmental Sciences, Cardiff University, Cardiff, UK, ³Geological Survey of Canada, 601 Booth Street, Ottawa, ON, K1A 0E8 *alanahinchey@gov.nl.ca https://orcid.org/0000-0003-3826-0724

Abstract

27

28

29

30

31

32

33

34

35

36

37

38

39

40

41

42

43

44

45

46

47

48

Gabbroic intrusions provide direct evidence of magmatic processes operating within the lithosphere and at the lithosphere-asthenosphere boundary, offering insights into magmatic differentiation, crustal growth, mantle-crust interaction, and tectonic evolution. The Taylor Brook Gabbro Suite (TBGS) is the northwesternmost expression of middle Silurian magmatism in the northern Appalachians. The petrogenesis and geochemical characteristics of the TBGS and crosscutting silicic magmatism are explored through U-Pb geochronology, mineral chemistry, lithogeochemistry, and Sr-Nd isotopic analyses, illustrating a complex history of mantle-derived mafic magmatism. The U-Pb zircon SHRIMP ages indicate that, although the intrusive history is complex, the TBGS represents a magmatic event at 431.0±2.7/4.3 Ma that was subsequently intruded by silicic magmatism at 419.7±3.0/4.5 Ma. The mineral chemistry and lithogeochemistry of the TBGS suggest fractional crystallization of a magmatic system as the primary differentiation mechanism. The TBGS is tholeiitic and transitional to calc-alkaline; consists of non-arc-like, continental magmas derived from an EMORB-like source. The silicic samples are granitic, magnesian and alkali calcic in composition. The isotopic signatures of the TBGS are mostly juvenile with εNd_(430 Ma) ranging from -1.1 to +6.4 and ⁸⁷Sr/⁸⁶Sr_(i) values ranging from 0.703373 to 0.708250; with one sample having an \(\epsilon\)Nd(430 Ma) of -8.6, indicating a minor role of crustal contamination by Mesoproterozoic to Neoproterozoic basement rocks. Magma ascent may have utilized inherited deep-crustal structures, such as the precursor to the Doucers Valley Fault/Long Range-Cabot Fault systems. Lithospheric extension likely caused by slab-rollback created a window that allowed for asthenospheric upwelling, inducing partial melting and generation of the TBGS magmas.

51

Keywords: Silurian Mafic Magmatism, Newfoundland, Appalachian orogen, Salinicorogeny, Gabbro

54

55

56

57

58

59

60

61

62

63

64

65

66

67

68

69

70

71

72

1. Introduction

The northern Appalachian orogen preserves the closing of the Iapetus and Rheic Oceans and their associated marginal seaways, leading to the collision of composite Laurentia and western Gondwana during the Alleghenian (Murphy et al. 2010; van Staal and Barr 2012; Waldron et al. 2022). Newfoundland preserves evidence of these ocean closures, as recorded by several orogenic cycles: Taconic, Salinic, and Acadian (see Hatcher 2010; Williams 1995). The late Silurian to middle Devonian (Salinic and Acadian) orogenic events resulted in extensive magmatism across Newfoundland, which is interpreted to have migrated across the orogen as a result of progressive shallowing of slab subduction (Murphy et al. 1999; van Staal and Barr 2012; van Staal et al. 2014; Wang et al. 2024). Newfoundland is dissected by major strike-slip to transtensional faults that are long-lived, complex, crustal-scale features that were initiated and reactivated throughout Appalachian orogenesis (Fig. 1). These faults controlled lateral, orogen-parallel transport of microcontinents and terranes (van Staal et al. 2021; Waldron et al. 2015). In western Newfoundland, the Long Range-Cabot Fault (LR-CF) system is thought to record major net dextral strike-slip movement (~200–300 km) of the Dashwoods terrane\Notre Dame are along the Laurentian margin during Ordovician to Carboniferous (Brem et al., 2007; Lin et al., 2013; van Staal and Zagorevski, 2020). Seismic reflection data support the interpretation that the LR-CF system is a crustal-scale discontinuity (i.e. deep transcurrent fault), which may have originated during oblique convergance and terrane accretion during Taconic to Acadian orogenesis (Barr et al. 2014; Stockmal et al. 1990; Waldron and Stockmal 1994). Inherited deep crustal structures have been shown to repeatedly serve as zones of deformation and reactivation during orogenesis (Guillaume et al. 2022; Hatcher 2010; Thomas 2006). The Laurentian margin is preserved in western Newfoundland as part of the Humber Zone and is separated by the LR-CF system from metamorphic equivalents of the marginal strata, interpreted to have been deposited on the hyperextended Laurentian margin and various microcontinents that are now preserved within the Notre Dame arc/Dashwoods terrane (Laurentian Realm; Fig. 1). The Doucers Valley Fault (DVF) system is a subsidiary of the LR-CF system and apparently controlled the emplacement of Ordovician ophiolitic slices (Southern White Bay Allochthon), deposition of Silurian cover sequences and focused Silurian magmatism in the White Bay region at the Humber margin-Dashwoods terrane boundary (Dunning 1987; Sandeman et al. 2024). This paper presents U-Pb geochronology, mineral chemistry, lithogeochemistry, and Sr-Nd isotopic data from Silurian magmatic rocks that intrude the Humber margin of Newfoundland along the DVF system. The mafic intrusive rocks are of particular interest because they provide petrological constraints on mantle sources and contemporaneous geotectonic evolution. Thus, these rocks can provide key insights into the mantle sources beneath the northeastern Appalachian segment of the continental crust. The objectives here are to: a) document the geology, petrology and ages of the magmatic rocks; b) elucidate the processes influencing their major and trace element compositions; c) describe the geochemical characteristics of the magma

73

74

75

76

77

78

79

80

81

82

83

84

85

86

87

88

89

90

91

92

93

sources; and d) evaluate the degree to which lithospheric/crustal contamination influenced the parental magmas.

2. Geological Setting

2.1. Regional Tectonic Framework

Historically, Newfoundland is divided from west to east into four tectonostratigraphic zones; namely, the Humber, Dunnage (Notre Dame/Dashwoods and Exploits terranes), Gander, and Avalon zones based on lithologic, paleontological, and lithogeochemical contrasts in pre-Silurian rocks (Fig. 1). The Gander and Avalon zones preserve remnants of different peri-Gondwanaderived terranes (Waldron et al. 2022). The Dunnage zone contains the remnants of various continental and oceanic arc terranes that formed ribbons in the Iapetus Ocean, either as peri-Laurentian tectonic elements (Dashwoods terrane/Notre Dame arc) or peri-Ganderian tectonic elements (van Staal and Zagorevski 2022). The Humber Zone (or margin, see van Staal and Barr 2012) preserves deformed early Paleozoic passive-margin successions that were deposited on Laurentia (on the western margin of the Iapetus Ocean), above Mesoproterozoic to early Neoproterozoic (Tonian) basement of the Grenville Province (Long Range Inlier; Fig. 2). The Taylor Brook Gabbro Suite (TBGS), the focus of this study, intrudes the Long Range Inlier and is described in detail in the subsequent section.

2.2. Geology of the Long Range Inlier

The Long Range Inlier of western Newfoundland comprises one of the largest exposures of Proterozoic crystalline rocks within the Appalachian orogen. It is not a simple stratigraphic inlier but represents a massif reactivated during Appalachian orogenesis. The approximately 8500 km² massif comprises the largest portion of the external Humber Zone (Owen 1991). The Long

Range Inlier forms a structural culmination bounded to the north, south and locally to the east by Proterozoic to Paleozoic cover rocks. The western boundary is marked by a southeast-dipping thrust fault (the Long Range frontal thrust) that placed (i.e. back thrust) Proterozoic crystalline rocks onto autochthonous Cambro-Ordovician platformal strata and Taconic allochthonous rocks (Erdmer and Williams 1995; Owen 1991). Paleozoic deformation of the inlier is marked by lowgrade metamorphism and tectonic overprinting along the DVF system and followed by emplacement of several intrusions, e.g., Devils Room granite, Gull Lake Intrusive Suite and the TBGS. The DVF system, a part of the LR-CF system, marks a wide tectonic zones of anastomosing ductile and brittle-ductile shear zones that are crosscut and overprinted by intense high-level brittle-ductile and brittle structures, largely obliterating the earlier ductile deformation structures. These faults and shear zones are long-lived, complex, crustal-scale features that were likely reactivated throughout the late Paleozoic assembly of the supercontinent Pangea (Hinchey et al. 2022; Hyde et al. 2007; Sandeman et al. 2024; Smyth and Schillereff 1982). Beginning in the Late Devonian, net dextral displacement along the LR-CF system is estimated at 200–300 km (Waldron et al. 2015). The Long Range Inlier is largely composed of amphibolite to granulite facies orthogneiss with minor paragneiss. Greenschist facies rocks increase in areal extent eastwards towards the DVF system. The geology is broadly divisible into the following tectonic divisions: 1) highgrade ca. 1530–1466 Ma Long Range Gneiss Complex; 2) weakly to strongly foliated late Grenvillian plutonic rocks defining two temporal periods (ca. 1032–1022 and 993–985 Ma); 3) mafic dykes (the ca. 615 Ma Long Range dyke swarm), 4) thin structural remnants of latest Neoproterozoic to Paleozoic cover sequences, and; 5) Early Silurian gabbroic intrusions and

118

119

120

121

122

123

124

125

126

127

128

129

130

131

132

133

134

135

136

137

138

minor silicic intrusions with volcanic equivalents (Fig. 1 & 2; Heaman et al. 2002; Hinchey 2020; Hinchey et al. 2025; Kamo et al. 1994; Owen 1991).

2.3. Silurian Magmatism

West of the DVF system, the only known expression of Silurian magmatism is the TBGS, with one thermal ionization mass spectrometry (TIMS) multigrain, U-Pb zircon age of 430.5 ± 2.5 Ma (Heaman et al. 2002) and the Devils Room granite (a poorly constrained, discordant, single bulk zircon age of 425 ± 10 Ma; Heaman et al., op. cit.). Aside from both intruding the Long Range Inlier, there is little previous research on either intrusion. East of the DVF system, there are Telychian (ca. 434 Ma) to Homerian (ca. 429 Ma) volcano-sedimentary rocks of the Sops Arm Group (Sandeman and Dunning 2016; Sandeman et al. 2024) as well as the Gull Lake Intrusive Suite that has a poorly constrained U-Pb TIMS age of $398 \pm 27/-7$ Ma (Erdmer 1986).

3. Methodology

This study integrates bedrock mapping, geochronology, petrography, thin section imagery, whole-rock lithogeochemistry, mineral chemistry and whole-rock Sr-Nd isotopic data. Representative samples were examined petrographically using polished thin sections. Details of the methodology are in supplemental material S1. Imaged thin sections (photomicrographs, Energy Dispersive X-ray Spectroscopy—Scanning Electron Microscopy—Mineral Liberation Analysis (SEM-MLA) maps and elemental maps) are presented in supplemental material S2 and Figure 4. The U-Pb sensitive high-resolution ion microprobe (SHRIMP) zircon data are reported in supplemental material S3, and sample locations are illustrated in Figure 3.

material S4. Mineral chemical analyses are presented in supplemental material S5. Major and trace element geochemical data are in supplemental material S6. Isotopic data are presented in supplemental material S7.

166

167

168

169

170

171

172

173

174

175

176

177

178

179

180

181

182

183

184

185

163

164

165

3.1. Silurian Magmatism – Field Mapping and Petrography

3.1.1. Taylor Brook Gabbro Suite (TBGS)

The northwest-oriented, oblong TBGS, mapped at a scale of 1:50,000, comprises three distinct phases: 1) a laterally extensive medium- to coarse-grained gabbro (unit 14: Fig. 2); 2) a coarse-grained to pegmatitic gabbro to melanogabbro (unit 15: Fig. 2), and; 3) a sporadically mappable phase of olivine gabbro to gabbronorite (unit 16: Fig. 2, Hinchey 2020). The most striking feature of the suite is its textural and compositional heterogeneity with abundant evidence of magma mingling (Fig. 3). Igneous layering is locally preserved (Fig. 3A & B), typically displaying moderate dips toward the centre of the body. However, the dip direction of this layering is not always consistent and locally dips outward. This may be the result of rotation associated with younger phases. The composite intrusion was originally termed the Taylor Brook Gabbro Complex (Owen 1991); however, Hinchey (2010) suggested renaming the intrusion to the TBGS as this would better reflect its compositional variability. Heaman et al. (2002) reported a physical abrasion, bulk zircon U-Pb zircon date of 430.5 ± 2.5 Ma from a fine-grained gabbro phase from the margin of the suite (Fig. 2). Because of its heterogeneity, it was questioned whether this age reflected the entirety of the TBGS, or if the Silurian age represented a younger, fine-grained mafic intrusion (Collins 2007).

Rocks of phase one (unit 14; Fig. 2) are medium- to coarse-grained, mesocratic gabbro and include minor gabbronorite, melanogabbro and norite phases (Fig. 4). The unit is

heterogeneous because of compositional variations at the centimetre scale. Along the margins of the intrusion, the gabbro is fine-grained. This phase typically preserves igneous layering and evidence for repetitive injection of magma and resultant magma mingling. Igneous layering varies from a few centimetres to a few metres in thickness and is highlighted by variations in grain size and mineralogy (Fig. 3B). Along the northwestern margin of the intrusion, the gabbro contains prominent flattened/compacted igneous layers occasionally defined by 2- to 10-cmthick discontinuous layers of massive magnetite (Fig. 3C). Locally spinel (hercynite)-rich layers define the igneous layering (Fig. 4B). This gabbroic phase has been intruded by medium-grained melanogabbro dykes that display chilled margins (Fig. 3C) and by other finer grained gabbroic dykes that are co-magmatic. Cognate and accidental xenoliths also occur. Dykes of leucocratic gabbro and locally clinopyroxenite are also found in the fine- and coarse-grained gabbro phases. Textures indicative of magma-mingling between leucocratic and melanocratic phases are also apparent (Fig. 3D). Plagioclase porphyritic gabbroic dykes that have chilled margins, cross-cut all units and are interpreted to represent the final pulses of gabbroic plutonism. Cumulate textures are apparent in the coarser-grained variants of this unit (supplemental material S2). Minor occurrences of disseminated sulphides, primarily pyrite and chalcopyrite, and magnetite are scattered throughout the intrusive phase (Fig. 4 & supplemental material S2). The second major intrusive unit (unit 15) is medium- to coarse-grained to pegmatitic hornblende gabbro to gabbronorite to melanogabbro that outcrops in the northern part of the complex (Fig. 2) and cuts fine-grained grey gabbro and melanogabbro that likely represent unit 14 (Fig. 3E). Unit 15 is coarse-grained to pegmatitic and contains pyroxene crystals up to 4 cm

long. The pyroxene is typically subhedral with cumulate textures locally preserved. The gabbro

and melanogabbro contain irregular patches that are enriched in plagioclase. Like the other

186

187

188

189

190

191

192

193

194

195

196

197

198

199

200

201

202

203

204

205

206

207

intrusive phases, this phase locally contains minor iron and copper sulphide (pyrite, chalcopyrite) minerals and magnetite. Comagnatic to late, fine-grained dykes of melanogabbro and locally clinopyroxenite 5–10 cm-wide cut unit 15 (Fig. 3F). The third mappable unit, olivine gabbro to gabbronorite (unit 16; Fig. 2), is coarse-grained (Fig. 3G) and occurs as small mappable bodies throughout the suite and also as outcrop-scale variations in unit 14. The unit preserves a cumulate texture and locally contains plagioclaseenriched patches (supplemental material S2). Disseminated magnetite and sulphide minerals occur locally. The unit is crosscut by finer-grained dykes of co-magmatic gabbro and leucogabbro. The TBGS is heterogeneous at all scales. The fluidity of the intrusive phases is indicated by syn-crystallization deformational features such as compacted igneous layering, dropped pendants that have disrupted igneous layers, magma mingling of leucocratic and melanocratic phases, multiple phases of non-chilled, irregular dyke emplacement and commonly repeated rock compositions (Fig. 3H). Modal abundance of magnetite is highly variable, with some units containing 2- to 5-cm-thick layers of massive magnetite to other phases that are virtually devoid of magnetite. The TBGS represents a laccolithic intrusion that intruded the Long Range Inlier (Fig. 3I & J). It is interpreted to have utilized pre-existing crustal-scale discontinuities, likely precursors to the DVG system, as a conduit for the multiple pulses of magma (Hinchey 2010). Thus, rather than representing a massive batholith, it is possibly a thinner sheet-like, composite intrusion. This would explain the large aerial extent of this pluton (>175 km²), which would otherwise have required a regionally extensive chamber to produce such a large batholith.

209

210

211

212

213

214

215

216

217

218

219

220

221

222

223

224

225

226

227

228

229

3.1.2. Silicic Magmatism

Two phases of silicic magmatism are spatially associated with the TBGS (Hinchey 2010, 2020). One forms leucocratic biotite monzogranite (unit 17; Fig. 2) dykes and sills that are locally large enough to be mappable (1:50,000 scale). These bodies are generally northeast-trending, range from 10 to 100 m in thickness, and are found intruding the pegmatitic gabbro to melanogabbro. The monzogranite is medium-grained (Fig. 3K), contains pegmatite patches and preserves 2- to 3-cm-wide chilled margins. The second phase of silicic magmatism is fine-grained quartz-feldspar porphyritic rhyolite dykes occurring in the southern portion of the intrusive suite (unit 18). These dykes are pink, have an aphanitic groundmass and contain euhedral, 1- to 4-mm-long quartz and alkali feldspar phenocrysts (Fig. 3L). Based on proximity, the silicic magmatism was suggested to be correlative with Silurian volcanic rocks of the Sops Arm Group, located east of the Long Range Inlier and the DVF system (Erdmer 1986).

4. U-Pb Geochronology

When using U-Pb SHRIMP data of Paleozoic zircon, the generally accepted age to report is in ²⁰⁶Pb/²³⁸U age (Black et al. 2003). This is because the ²⁰⁷Pb counts in young zircon are low and highly sensitive to the assumed common lead composition, leading to extremely large uncertainties in individual analyses. As a result, the ²⁰⁷Pb/²⁰⁶Pb age estimates carry significant uncertainty, rendering discordance calculations and there ages difficult to interpret. Typical data treatment for Phanerozoic zircon is to plot the results uncorrected for common Pb, without the additional common Pb correction uncertainty, on a Tera-Wasserburg diagram and evaluate its collinearity. The collinear data represent a single age population with varying degrees of common Pb.

4.1. Hornblende Gabbro (09AH369A; GSC lab number 10144)

254

255

256

257

258

259

260

261

262

263

264

265

266

267

268

269

270

271

272

273

274

275

276

A sample from a very coarse-grained, cumulate-textured, hornblende gabbro from unit 14 was collected for analysis (Figs. 2, 5A & B). In outcrop, the hornblende gabbro is compositionally heterogeneous and includes minor patches that grade into leucogabbro, gabbro and norite. Amphibole comprises over 50% of the rock, with three distinct phases of growth. In the first phase, magnesio-hornblende replaces clinopyroxene. The second phase is subhedral pargasite. In the third phase, small acicular pargasite grains grow around the earlier pargasite (Fig. 5C & D). The sample yielded abundant colourless to pale brown anhedral zircon (Fig. 6A). Some grains are prismatic and may rarely contain inclusions. In CL images, the grains are strongly luminescent and exhibit straight oscillatory zoning (supplemental material S4). A total of 25 zircon grains, varying in shape and internal structure, were analyzed. Thirty-two analyses resulted in ²⁰⁶Pb/²³⁸U dates (²⁰⁷Pb-corrected) from 413 to 452 Ma with an additional 2 grains yielding Grenvillian ages (999, 1102 Ma; supplemental material S3). All the grains, including the Grenvillian-aged ones, are characterized by low U (less than 100 ppm, most less than 50) and high Th/U (0.6–1.2). Both the andehdral/fragmental morphology and chemistry of the zircon grains are consistent with what is commonly observed in mafic plutonic rocks (Heaman and LeCheminant 1993; Heaman et al. 1990). A weighted mean ²⁰⁶Pb/²³⁸U age of 431.0 \pm 2.7/4.3 Ma (2 σ uncertainties internal/external, ²⁰⁷Pb-corrected, n=26, MSWD = 1.3, probability of fit = 0.05) was calculated using analyses with the lowest common Pb (uncorrected 207 Pb/ 206 Pb <0.12) to minimize the effect of the correction on the age (Fig. 6A). This is interpreted as the crystallization age of the hornblende gabbro. The Grenvillian age zircons are interpreted as inherited.

4.2. Monzogranite (09AH368A; GSC lab number 10146)

277

278

279

280

281

282

283

284

285

286

287

288

289

290

291

292

293

294

295

296

297

298

299

This sample is from a leucocratic, fine-grained, biotite monzogranite (unit 17; Fig.2, 5E & F) that cuts unit 15. In thin section, plagioclase, quartz and potassium feldspar are predominant phases with muscovite, epidote, chlorite, biotite and magnetite as accessory phases (Fig. 5G & H). Some plagioclase grains contain sericite alteration. Evidence for minor post-crystallization deformation includes deformed undulose extinction in interstitial quartz and irregular, crosscutting, plagioclase polysynthetic twinning. Approximately 40 zircon grains were mounted. Most grains are sharply faceted ranging from equant and stubby prism to elongate with aspect ratios of 4:1 (Fig. 6B). Fluid inclusions and inclusions of other minerals are common. Most grains are strongly luminescent in CL, consistent with relatively low U content but a small number of grains have poor CL response, suggesting high U or older ages (supplemental material S4). A total 24 analyses were carried out on 17 zircon grains with variable shapes and internal structures. Twenty analyses resulted in ²⁰⁶Pb/²³⁸U dates (²⁰⁷Pb-corrected) from 392 to 437 Ma (supplemental material S3). These were all from relatively low U zircon (less than 200 ppm) with the exception of one high U grain (3500 ppm), which returned the oldest age. High U grains are known to return anomalously old ages due to matrix effects during sputtering (White and Ireland 2012) and thus this analysis will not be considered in further discussions. The weighted mean ²⁰⁶Pb/²³⁸U age of 21 analyses is 419.7±3.0/4.5 Ma (2σ uncertainties internal/external, 207 Pb-corrected n = 20, MSWD = 1.9, probability of fit = 0.01) which is interpreted as the age of the monzogranite (Fig. 6B). Two analyses were excluded on statistical grounds using the "autoreject" function of Isoplot4.15 (Ludwig 2012). Additional analyses on the same grain fall within the igneous population suggesting that these two slightly younger

results may have been affected by Pb-loss. A comparison of the ages and the internal uncertainties is only appropriate when comparing the monzogranite and the gabbro in this report since they were analysed during the same analytical session. When comparing with other datasets the external uncertainty must be used.

5. Mineral Chemistry, Whole-rock Lithogeochemistry and Isotopic Chemistry

Mineral chemical analyses of nine samples of the TBGS were completed (supplemental material S5). Representative lithogeochemistry for thirty diverse samples of the TBGS, and four samples of monzogranite and two samples of rhyolite were analyzed (supplemental material S6). Table 1 provides a summary of select major- and trace-element ratios. A subgroup of nine samples was subsequently analyzed for whole-rock Sr and Nd isotopic compositions (supplemental material S7).

5.1. Mineral Chemistry (TBGS)

Olivine grains are compositionally unzoned and uniform on the sample scale. The Mg# in olivine (Mg# = 100 x molecular MgO/MgO+FeO^T) ranges from 67.0 to 77.1 with an average of 72.4 (Fig. 7A). Except for one gabbro sample, plagioclase ranges from bytownite (An₇₅₋₄₁Ab₅₈₋₂₄Or₀₋₂) to oligoclase (An₃₉Ab₅₉Or₂; Fig. 7B). One sample plots in the albite field (An₁₋₂Ab₉₇₋₂₉Or₁), likely reflective of alteration. Clinopyroxene has variable compositions between samples, although samples do not show systematic zoning in individual grains. Samples plot in two distinct groups, regardless of rock type. One group straddles the diopside to augite boundary (Fig. 7C), whereas the second group plots in the augite field with Wo₃₀₋₅₀En₃₃₋₅₀Fs₂₀₋₂₅. The Mg# values of clinopyroxene range from 60.5 to 98.9. Orthopyroxene ranges from enstatite to ferrosilite (Fig. 7C) with Wo₁₋₄En₃₋₇₈Fs₃₇₋₇₆ and Mg# values ranging from 39.1 to 80.1.

Amphiboles are part of the calcic group with Mg# values of 45.9–82.7, and can be further classified as ranging from Ti-rich pargasite to magnesian hornblende (supplemental material S5). Accessory phases typically comprise rutile, spinel (hercynite), magnetite and ilmenite (supplemental material S2 & S5).

328

329

330

331

332

333

334

335

336

337

338

339

340

341

342

343

344

345

346

324

325

326

327

5.2. Major and Trace Element Geochemistry

5.2.1. Taylor Brook Gabbro Suite

Based on their major and trace element chemistry, the TBGS samples (n=26) form two distinct geochemical groups that largely correlate with the lithological units. Group A comprises samples from units 15 and 16 that primarily occur in the central body of the intrusion (Fig. 2). Group A has SiO₂ contents ranging from 45.6–49.3 wt%, with Al₂O₃ from 18.1–22.7 wt%, CaO from 9.3–13.8 wt% and MgO from 5.3–12.3 wt% (supplemental material S6). Group A exhibits moderate to high Mg# (57–76) and low TiO₂ concentrations ranging from 0.2–0.6 wt%, except for one sample that has 1.8 wt% TiO₂. Group B in contrast has relatively lower SiO₂ (42.2–48.5 wt%), Al₂O₃ (11.9–17.5 wt%), CaO (6.9–13.5 wt%) and MgO (4.1–8.4 wt%). Group B samples are from unit 14 which comprises most of the areal extent of the intrusion. Group B rocks exhibit low to moderate Mg# (35–60) and high TiO₂ concentrations ranging from 1.6–3.9 wt%. Various major and trace elements are plotted against Mg# (Fig. 8) to illustrate fractionation trends. Both Ni and Cr decrease with decreasing Mg# (not illustrated). Group A samples show a clear trend of being less fractionated compared to the more evolved compositions of Group B (Fig. 8). On a total alkali-silica classification diagram, both groups largely plot in the gabbro field (Fig. 9A). However, the distinction between the less fractionated Group A samples from the more evolved Group B is illustrated on a Jensen cation plot (Fig. 9B).

Primitive mantle normalized (Sun and McDonough, 1989) incompatible multi-element profiles of Group A rocks (Fig. 10A) are characterized by a slight enrichment in incompatible elements relative to primitive mantle, with concave-down to fractionated light rare earth element profiles (LREE; (La/Sm)_{pm}= 0.50–2.2; the subscript pm refers to primitive mantle normalized values). In addition, the group displays variable multi-element profiles with flat to slightly fractionated heavy-rare earth element (HREE) profiles ((Sm/Yb) $_{pm}$ = 1.33–2.1), and variably positive to negative Zr, and Ti anomalies and consistently positive Eu anomalies. On chondrite normalized REE diagrams, Group A shows flat to moderately steep slopes ((La/Yb)_{cn}= 0.8–3.8; the subscript on refers to chondrite normalized values; Sun and McDonough, 1989) and strong positive Eu anomalies (Eu/Eu*=1.4–2.2; Fig. 10B). In comparison, Group B is significantly enriched in all incompatible elements relative to primitive mantle and to Group A; displaying flat to fractionated LREE ((La/Sm)_{pm}= 1.0–2.4). The group also displays flat to strongly fractionated heavy-rare earth element (HREE) profiles $((Sm/Yb)_{pm} = 1.0-4.3)$ with predominantly positive Zr anomaly and an absence of Eu anomalies (Fig. 10C). On REE diagrams, Group B shows flat to moderately steep slopes and negligible Eu anomalies (Eu/Eu*=0.8-1.2; Fig. 10D), and typically shows stronger degrees of REE fractionation ((La/Yb)_{cn}= 1.0–7.5).

5.2.2. Silicic samples

347

348

349

350

351

352

353

354

355

356

357

358

359

360

361

362

363

364

365

366

367

368

369

Four monzogranite and two rhyolite samples have similar geochemistry will be treated as one group. They have narrow ranges of SiO₂ (75.5–76.0 wt%), Al₂O₃ (13.1–14.0 wt%) and Na₂O (3.9–4.6 wt%) concentrations and plot as rhyolites on a total alkali-silica classification diagram (Fig. 9A). On a Jensen cation plot, the samples plot in the granite field (Fig. 9B). The samples plot as magnesian, metaluminous, and alkali calcic in composition (Fig. 9C). They have variable Zr/Nb (1.8–6.0) and Zr/Y (1.7–11.4) and high Al₂O₃/TiO₂ ratios (148.4–236.9; Table 1).

Primitive mantle normalized incompatible multi-element profiles of the samples (Fig. 10E) are enriched in all incompatible elements relative to primitive mantle, with moderate to strongly fractionated LREE ((La/Sm)_{pm}= 0.9–5.8). In addition, the samples have flat to moderately fractionated HREE profiles ((Sm/Yb)_{pm} = 0.5–1.7), Nb depletion relative to Th ((Nb/Th)_{pm} = 0.2–0.5; Table 1), and Nb peaks relative to La ((Nb/La)_{pm} = 1.3–5.7; Table 1). They have Δ Nb values that range from 0.2 to 1.2 (Table 1). On chondrite normalized REE diagrams, the samples are characterized by moderate REE fractionation ((La/Yb)_{cn}= 1.3–5.9), and have moderate to strong negative Eu anomalies (Eu/Eu*=0.1–0.9; Fig. 10F).

5.3. Sr and Nd Isotopic Chemistry

Samples of TBGS and silicic rocks were analyzed for whole-rock Sr and Nd isotopes (supplemental material S7). Not all samples yielded Sr isotopic ratios. Initial epsilon Nd and ⁸⁷Sr/⁸⁶Sr values were calculated using an age of 430 Ma. The initial ⁸⁷Sr/⁸⁶Sr ratios of Group A gabbros range from 0.703373 to 0.703887; Group B samples range from 0.702177 to 0.708250 and the silicic rocks range from 0.702124 to 0.713472. The Group A samples ¹⁴³Nd/¹⁴⁴Nd range from 0.512642 to 0.512858 with corresponding εNd_(t=430 Ma) = +1.3 to +4.3. The Group B samples have ¹⁴³Nd/¹⁴⁴Nd that range from 0.511944 to 0.512915 and corresponding εNd_(t=430 Ma) values that range from -8.6 to +6.4. The silicic samples have ¹⁴³Nd/¹⁴⁴Nd ranging from 0.512320 to 0.512612, εNd_(t=430 Ma) values that range from -3.7 to -0.7. The depleted mantle εNd value at 430 Ma is +9.32 (Goldstein et al. 1984) or +7.26 (DePaolo 1988). The range in εNd_(t=430 Ma) values for all of the samples could indicate that they were derived from a LREE-enriched mantle source, or that they have experienced variable amounts of lithospheric contamination.

6. Discussion

392

393

394

395

396

397

398

399

400

401

402

403

404

405

406

407

408

409

410

411

412

413

414

6.1. Petrogenesis of the TBGS

6.1.1. Crustal Contamination and Crystal Fractionation

The TBGS samples have relatively low LOI values (supplemental material S6; LOI = 0.31– 2.22 wt%) and rarely have visible alteration in petrographic analysis. This indicates that postemplacement changes in the geochemical signatures are unlikely. The TBGS contains low SiO₂ coupled with high MgO, Fe₂O₃^T, Cr and Ni indicating that the magma was derived from a mantle source. Mantle-derived magmas can be prone to crustal contamination, leading to an increase in incompatible elements like Th, Pb, La, Ce, Zr, LREE and Hf and a decrease in Nb-Ta in derivative magmas (Rudnick and Gao 2003; Sun and McDonough 1989). Neither gabbro group of the TBGS exhibits marked increases in the incompatible elements nor a prominent Nb anomaly, suggesting that crustal contamination did not play a significant role in the formation of the TBGS (Fig. 10). However, the TBGS intrudes Grenvillian basement rocks which have strongly negative εNd_t values (Dickin 2004), and TBGS samples plot between the depleted mantle and the basement rocks suggesting minor contamination by older continental lithosphere (Fig. 11). This is consistent with the minor amount of Grenvillian zircon inheritance observed in the U-Pb results (supplemental material S3). As Sm and Nd are incompatible elements and more abundant in crustal rocks than in the mantle, even minor contamination of a mantle melt by older continental lithosphere will disproportionately control the ENd and model ages of the mantlederived melts (Moyen et al. 2021). The TBGS displays a range of textures from adcumulate to orthocumulate. These cumulate textures result from solid-liquid separation processes, as indicated by modal and grain-size layering at scales ranging from millimetres to decimeters (Fig. 4 & supplemental material S2).

Such textures suggest fractional crystallization/accumulation as the primary differentiation mechanism of the magmas. Therefore, the variation in the major and trace-element composition of the rocks is largely controlled by the cumulate phases. SiO₂ varies little, whereas Co exhibits a negative correlation with Mg#, indicative of olivine fractionation (Fig. 8A & B). Plagioclase is the predominant cumulate mineral in Group A rocks, and their whole-rock Al₂O₃ contents reflect the effects of early plagioclase fractionation or accumulation under reducing conditions, where Fe²⁺ is stable in melt favouring plagioclase crystalization (Fig. 8C). A consistently strong positive Eu anomaly also highlights the cumulate nature of this group (Fig. 10B). In contrast, negligible Eu anomalies in the Group B samples suggest a shift in redox conditions from reducing to oxidizing leading to the stabilization of Eu³⁺ (Fig. 9D, Cicconi et al. 2021; Terakado and Fujitani 1995). Alternatively, changes in fractional crystallization could also influence the stability of Eu³⁺ (Holder et al. 2020). Similarly, the Eu troughs in the silicic samples suggest that plagioclase removal likely influenced their compositions (Fig. 10F). The impact of plagioclase fractionation can be seen in trace-element ratio diagrams (Fig. 8). The accumulation of plagioclase and the positive Eu anomalies in Group A rocks are indicative of low H₂O contents in the melts, as high H₂O contents can inhibit plagioclase accumulation (Müntener et al. 2001). In Figure 8D, the Sr/Y trend is largely attributed to plagioclase accumulation in the cumulate Group A samples. The negative correlation of Mg# and Sc and CaO/Al₂O₃ supports pyroxene fractionation (Fig. 8E & F). The Fe-Ti oxides (magnetite and ilmenite) are also major phases in the gabbroic rocks, and their crystallization strongly influences the whole-rock FeO and TiO₂ contents of TBGS (Fig. 8G & H). As Zr appears to be controlled almost entirely by fractionation, increasing Ti/Zr ratio indicates the accumulation of ilmenite/titanite (Fig. 8H). The TGBS rocks display notable consistent Dy/Yb ratios, indicating insignificant amphibole fractionation (Fig.

415

416

417

418

419

420

421

422

423

424

425

426

427

428

429

430

431

432

433

434

435

436

8I). This is also supported by the amphibole mineral chemistry classifying almost exclusively as pargasite (supplemental material S5).

Concentrations of incompatible elements, such as La, Sm, and Yb, typically vary significantly during partial melting due to their preferential incorporation into the melt. In contrast, these elements show less variation during fractional crystallization, as they remain relatively enriched in the melt while the crystallizing mineral phases primarily exclude them. The TBGS samples show increasing La/Sm and La/Yb as La content increases (Fig. 12A & B), indicating progressive incompatible element enrichment during magmatic differentiation, supporting the role of fractional crystallization of the magma.

6.1.2. Mantle Source Components

Mantle source components of the TBGS can be interpreted using incompatible trace element ratios that are relatively unaffected by fractional crystallization or partial melting. The TBGS samples have E-MORB to OIB chemical affinities, including elevated (La/Yb)_{en} and negligible Nb, Ti and Eu anomalies on extended trace element and REE diagrams (Fig. 10). The samples typically plot near E-MORB on trace element discrimination diagrams (Fig. 13A & B). They exhibit low (Tb/Yb)_{en} ratios (Fig. 13C), which indicate relatively small melt fractions and/or the absence of garnet in the source melt, suggesting that the melting occurred in the spinel stability field, at depths typically less than 80 km (Zhang et al. 2008). Moreover, the TBGS samples display moderate (La/Sm)_{pm} (largely >1), which, when interpreted together with the REE patterns, supports their derivation of the primary melts of the TBGS from modest degrees of partial melting of an enriched mantle source (Fig. 13D).

The isotopic signatures for the TBGS are mostly juvenile with $\epsilon Nd_{(430 \, Ma)}$ ranging from -1.1 to +6.4 and ${}^{87}Sr/{}^{86}Sr_{(i)}$ values ranging from 0.703373 to 0.708250; with one sample having an $\epsilon Nd_{(430 \, Ma)}$ of -8.6 (Fig. 11). Their isotopic variability may either reflect variability in the mantle source, or alternatively, a role for minor lithospheric contamination. Their collective geochemical compositions are consistent with their primary derivation from an enriched mantle source.

460

461

462

463

464

465

466

467

468

469

470

471

472

473

474

475

476

477

478

479

480

481

E-MORB compositions are believed to originate from a depleted asthenospheric mantle that has been refertilized by enriched components related to subduction, or they may also represent a lower degree of partial melting of an N-MORB mantle source (Saccani et al. 2013). The (Th/Ta)/(Th/Tb) ratios for the TBGS are <1 and are typical of N-MORB-derived rocks (Allègre and Minster 1978). This could suggest that the TBGS formed from an N-MORB-like source. However, N-MORB compositions typically have low (La/Yb)_{pm} and (Sm/Yb)_{pm} ratios and those for the TBGS are much higher, negating the possibility of partial melting of an N-MORB mantle source. The TBGS samples show LREE/HREE enrichment and have greater LREE enrichment than that of N-MORB (Fig. 10D) indicative of an E-MORB mantle source. The predominantly positive $\varepsilon Nd_{(430 \text{ Ma})}$ values observed in the samples are generally consistent with a relatively depleted mantle source; however, on trace element ratio diagrams they plot towards a more enriched mantle source (Fig. 13A & B). Mantle plume enrichment is typically associated with an OIB chemical signature. This suggests the source for the TBGS is a depleted asthenospheric mantle that has been refertilized by subduction zone enrichment. This dual influence produces a mixed geochemical signature, combining characteristics of both depleted (e.g., high ENd) and enriched mantle components (e.g., elevated incompatible element ratios; Fig. 13D).

6.2. Petrogenesis of the Silicic Rocks

482

483

484

485

486

487

488

489

490

491

492

493

494

495

496

497

498

499

500

501

502

503

504

The silicic samples are all granitic and display negative Nb, Ti and Eu anomalies, signatures typically associated with crustal-derived melts. They are magnesian, metaluminous and alkali calcic in composition (Fig. 9C). Depletion of Nb and Ti are interpreted as arc-type signatures in silicic rocks but can also arise from the anatexis of rocks with arc parentage (Morris and Ryan 2003; Whalen et al. 1998) or through lithospheric contamination of a mantle-derived melt. In silicic magmas, an abundance of large ion lithophile elements (LILE) and elevated LREEs are typically attributed to the input of fluids or melts derived from crustal sources, related either to subduction processes or to intra-crustal contamination (Zamboni et al. 2016). On multi-element and REE plots, the silicic rocks have patterns typical of melts derived by partial melting of a sialic crust (Fig. 9E & F; Brewer et al. 2004; Menuge et al. 2002). The εNd_(t=430 Ma) values for the silicic rocks plot between depleted mantle and Grenvillian basement (Fig. 11), suggesting minor involvement of Grenville crust in their genesis. The silicic samples have elevated Y and Yb_(CN) but low Sr/Y and (La/Yb)_{CN} (supplemental material S6), a classic signature of fractional crystallization of an intermediate melt (e.g., tonalitic) under shallow crustal conditions where plagioclase and amphibole dominate the mineral assemblage, but garnet is absent (Drummond and Defant 1990; Drummond et al. 1996). This suggests that the silicic samples are derived in part via partial melting and/or assimilation of minor amounts of Grenvillian basement rocks of the Long Range Inlier. The silicic magmatism has been proposed to be correlative with the Sops Arm Group silicic volcanic rocks (Heaman et al. 2002). The new geochronology data presented herein suggest that

the granitic magmatism is ~ 10 m.y. younger than the Sops Arm Group. The ca. 419 Ma age of

magmatism is the youngest Silurian magmatism known in the area. Magmatism of this age is

documented throughout Ganderian margin (see Wang et al. 2024). Whether the quartz-feldspar porphyry rhyolites are synchronous with the Sops Arm Group or the younger ca. 419 Ma magmatism remains unknown.

6.3. Timing of Silurian Magmatism

505

506

507

508

509

510

511

512

513

514

515

516

517

518

519

520

521

522

523

524

525

526

The TBGS intruded the Laurentian margin into the Mesoproterozoic to Neoproterozoic (Tonian) basement of the Long Range Inlier. The geochronological data presented herein indicates that although TBGS is multiphase and the intrusive dynamics and history is complex, the timing of intrusion is well constrained to 431.0±2.7/4.3 Ma; overlapping with previously reported bulk zircon physical abrasion TIMS zircon age from a fine-grained phase along the margin of the intrusion at 430.5 ± 2.5 Ma (Heaman et al., 2002). Therefore, despite the heterogeneous, multiphase intrusive history of the TBGS, it appears to represent a short-lived magmatic event. The cross-cutting silicic magmatism is constrained to 419.7±2.7/4.3 Ma. The extent of this silicic magmatic event in the Long Range Inlier is unknown. Still, it may be related to other poorly temporally constrained intrusive units in the region (e.g., Gull Lake Intrusive Suite or Devils Room Granite). This ca. 430 Ma (Homerian) magmatic event has been documented east of the TBGS in both the peri-Laurentian and peri-Gondwanan segments of the Dunnage Zone (Dunning et al. 1990; Lissenberg et al. 2006; Sandeman et al. 2024; Wang et al. 2024). This confirms that a Homerian asthenospheric upwelling, likely driven by slab-rollback, is recognized in western and central Newfoundland (Sandeman et al. 2024; van Staal et al. 2014; Whalen et al. 2006). This Homerian magmatic event is also documented along the entire northern Appalachian orogen (Castonguay et

al. 2014; Dorais et al. 2017; Karabinos et al. 2008; Rankin et al. 2007; Wilson et al. 2017).

6.4. Geodynamic Implications

527

528

529

530

531

532

533

534

535

536

537

538

539

540

541

542

543

544

545

546

547

548

549

In western Newfoundland, the LR-CF system is interpreted to record major net dextral strikeslip movement of the Dashwoods terrane\Notre Dame arc along the Laurentian margin during Ordovician to Carboniferous (Brem et al., 2007; Lin et al., 2013; van Staal and Zagorevski, 2020). Restoration of movement along these faults amounts to between 200-300 km of slip (Waldron et al. 2015), indicating that during the Silurian, the Long Range Inlier was proximal to the southern Dashwoods or perhaps farther southwest (present-day orientation). The nature of the LR-CF system as a crustal-scale discontinuity that extends into the upper mantle is evidenced by seismic reflection data supporting the interpretation that the LR-CF system is a deep transcurrent fault, which formed during oblique convergance and terrane accretion during Taconic to Acadian orogenesis (Barr et al. 2014; Stockmal et al. 1990; Waldron and Stockmal 1994). Inherited deep crustal structures repeatedly serve as zones of deformation and reactivation during orogenesis (Guillaume et al. 2022; Hatcher 2010; Thomas 2006). In regions characterized by inherited deep crustal structures, such as the DVF/LR-CF systems, mafic magmatism can be driven by a combination of transtensional tectonics, lithospheric extension and rifting, and reactivation of pre-existing structural fabrics (Matton and Jébrak 2009). Continental-scale strike-slip faults and shear zones in orogenic belts typically develop as a result of the continuing movement of foundational lithospheric blocks (terranes) within the developing orogen. The strike-slip faults in western Newfoundland, such as LRCF system, for the most part follow the boundary zone between lithosphere of differing thickness, age and internal structure and represent major crustal and lithospheric discontinuities that likely constitute corridors/conduits along which mantle melts can ascend or flow laterally along (Murphy 2003; Pirajno 2010; Rocchi et al. 2003). These melts would eventually be focused at

the mantle-crust and lithosphere-asthenosphere boundaries. Although a seismic lithoprobe line across the LR-CF system in the southern Humber zone indicates a boundary zone of differing lithospheric thickness (Brem 2007; van der Velden et al. 2004), whether this difference is reflected across the DVF system is unknown. During the late Silurian, and immediately after the terminal Iapetan closure, amalgamated Laurentian, peri-Laurentian and peri-Gondwanan terranes (excluding Avalonia) of the Newfoundland Appalachians record voluminous, largely bi-modal, eastward-younging and extension-related, non-arc-like magmatism attributed to slab rollback or breakoff (Honsberger et al. 2022; Lissenberg et al. 2006; Sandeman et al. 2024; van Staal et al. 2014; Whalen et al. 2006). The formation of the TBGS is inferred to be contemporaneous with this magmatic event, indicative of extension in the upper plate (Laurentian margin). Extension in the eastern Humber/Laurentian margin would likely have utilized preexisting structures. Slab rollback would create a window beneath the extending upper plate, allowing local asthenospheric upwelling, which introduced heat and partial melting of the subcontinental lithospheric mantle. The precursor to the DVF system would have enabled locally focused, decompressional partial melting and subsequently acted as a pathway(s) for the ascent of derivative mafic magmas of the TBGS. The TBGS laccolith formation may have been focused in the area because of ponding of the magma batches near the structural brittle-ductile transition zone along a NW-trending fault zone conjugate to the DVF and LR-CF systems. This is the only known occurrence of

magmatism of this age in the Long Range Inlier of Western Newfoundland.

550

551

552

553

554

555

556

557

558

559

560

561

562

563

564

565

566

567

568

569

570

7. Conclusions

571

572

573

574

575

576

577

578

579

580

581

582

583

584

585

586

587

588

589

590

591

592

593

Field, petrographic, U-Pb geochronological data, mineral chemistry, and lithogeochemical and isotopic data for the TBGS provide new insights into Silurian magmatism in the Laurentian margin of western Newfoundland. The TBGS is a multiphase, heterogeneous, cumulate, NWtrending oblong body that intrudes the Proterozoic Long Range Inlier. The complex, co-mingling relationships along with the U-Pb zircon SHRIMP ages indicate that although the intrusion contains multiple phases, the gabbroic components of the suite represent a single brief magmatic event at ca. 431.0±2.9/4.3 Ma that was subsequently intruded by slightly younger, minor silicic magmatism at 419.7±3.0/4.5 Ma. Mineral chemical and lithogeochemical data indicate that the predominant control on compositional evolution of the rocks of the TBGS was fractional crystallization of olivine+clinopyroxene+feldspar and Fe-Ti oxides. The suite is tholeiitic and transitional to calc-alkaline, non-arc-like, continental magmas derived from an E-MORB-like source. This is supported by the largely positive $\varepsilon Nd_{(430Ma)}$ ratios and primitive Sr isotopic compositions. The silicic samples are granitic, magnesian and alkali calcic in composition, likely reflecting partial melting and/or assimilation of feldspathic, meta-igneous middle to upper crustal Proterozoic basement rocks. The ~10-million-year age gap between mafic and silicic magmatism indicates that the silicic magmatism is not likely a direct result of mafic magmatism melting the crust, although this cannot be ruled out. Following the terminal closure of the Iapetus Ocean and associated seaways, the TBGS formed as a result of extension tectonics along the Laurentian margin. Slab rollback would have created a window beneath the extending upper plate, promoting local asthenospheric upwelling, which introduced heat and partial melting of the subcontinental lithospheric mantle. The precursor to the DVF system, a zone of inherited structural weakness, would have facilitated

localized adiabatic decompressional melting within the upper asthenosphere and subsequently acted as a pathway(s) for the ascent and emplacement of mantle-derived mafic magmas.

596

597

598

599

600

601

602

603

604

594

595

Acknowledgements

This research was funded by the Geological Survey of Newfoundland and Labrador (GSNL). Kim Morgan and Evie Li are thanked for their cartographic support. Internal reviews by colleagues at the Geological Survey (Gabriel Santos and Chris Pereira) and Geological Survey of Canada (Bill Davis) greatly improved the clarity of the manuscript. External reviews by Cees van Staal and two anonymous reviewers further improved the manuscript. Comments and handling of the manuscripts by Editor Sally Perhsson were equally appreciated. All whole-rock geochemical data are available from the GSNL Geological Atlas, located here: https://geoatlas.gov.nl.ca and in the supplemental material sections.

606 607

605

Figure Captions

- 608 **Figure 1**. Simplified geological map of Newfoundland showing the location of the Taylor Brook
- 609 Gabbro Suite relative to major geological terranes and tectonic boundaries. The location of the
- Long Range Inlier relative to the Grenville Province in eastern Labrador is illustrated in the inset
- 611 map. Beothuk Lake Line (BL, formally Red Indian Line) nomenclature is from van Staal et al.
- 612 (2024). Abbreviations: BDF, Baie d'Est Fault; DVF, Doucers Valley Fault system; DRG, Devils
- Room granite; GBF, Green Bay Fault; GHF, Gunflap Hills Fault; GL, Gander Lake subzone;
- LRI, Long Range Inlier; MC, Mount Cormack subzone; MMLg, Mic Mac Lake Group; MP,
- Meelpaeg; NAF, Northern Arm Fault; NPL, Noel Paul's Line; TBGS, Taylor Brook Gabbro
- Suite; Vlsz, Valentine Lake shear zone; Sz, subzone; . Modified after Colman-Sadd et al. (1990);
- 617 Hinchey (2010); Sandeman et al. (2024).

- Figure 2. Geology of the Silver Mountain map area. Modified after Hinchey (2020). U/Pb zircon
- ages from Heaman et al. (2002) and this study.

621	
622	Figure 3. Field photographs A) Igneous layering in the TGBS, illustrating planar compositional
623	changes from leucocratic hornblende gabbro to melanocratic pyroxene hornblende gabbro.
624	Layering is offset by late (Acadian?) brittle faulting (09AH002). B) Dm-scale igneous layering
625	of leucogabbro, pyroxene-hornblende gabbro, plagioclase porphyritic layers, magnetite-rich
626	layers (black), and spinel-rich layers cut by a fine-grade melanogabbro (09AH143). C)
627	Melanogabbro dyke with chilled margin cutting magnetite-rich layers alternating with
628	plagioclase-enriched versus clinopyroxene-enriched layers. D) Magma mixing textures between
629	coarse-grained, homogenous gabbronorite and fine-grained melanogabbro. E) Megacrystic
630	gabbro that brecciated three other phases composed of coarse-grained melanogabbro, fine-
631	grained black hornblende gabbro and fine-grained melanogabbro (09AH308). F) Pegmatitic to
632	very coarse-grained gabbro to melanogabbro cut by dykelettes of fine-grained grey gabbro
633	(09AH319). G) Coarse-grained, homogenous gabbronorite with cumulate texture (09AH146). H)
634	Contact between fine-grained monzogranite with chilled margins against variably textured
635	gabbro (09AH368). I) Melanogabbro intruding a foliated granitic Grenvillian Pluton. J) Gabbro
636	with xenoliths of the Long Range Gneiss complex. K) Medium-grained, monzogranite
637	(09AH303). L) Quartz-feldspar porphyry rhyolite (09AH278). Mag, magnetite; Amp,
638	Amphibole; F. gr., Fine-grained; C. gr., Coarse-grained; Opx, orthopyroxene; Cpx,
639	clinopyroxene; LRGC, Long Range Gneiss Complex.
640	
641	Figure 4. Scanning Electron Microscopy-Mineral Liberation Analysis images with semi-
642	quantitative weight percentages and photomicrographs of the samples. Top left, plane polarized
643	light; bottom right, cross polarized light. A) & D) Olivine gabbro – Group A, B) & E) Gabbro –
644	Group B (hercynite-rich layer), and C) & F) Pyroxene hornblende gabbro - Group B. Mag,
645	magnetite; Opx, orthopyroxene; Pl, plagioclase; Hc, hercynite; Cpx, clinopyroxene; Ol, Olivine;
646	Hbl, Hornblende.
647	
648	
649	Figure 5. Field photographs (A & B) and photomicrographs (C & D) of the melanogabbro
650	(09AH369A) collected for U-Pb zircon analysis. Field photographs (E & F) and
651	photomicrographs (G &H) of the monzogranite (09AH368A) collected for U-Pb zircon analysis.

652 Prg, pargasite; Mhb, magnesiohornblende; Qt, quarts; Kfs, potassium feldspar; Pl, plagioclase. 653 654 Figure 6. Tera-Wasserburg concordia diagrams of Pb-U results from this study. Data plotted is 655 uncorrected for common Pb, whereby the offset from the concordia curve is a reflection of the proportion of common Pb using the ²⁰⁷Pb-method. Ellipses shown in red are used in the 656 657 calculation of the crystallization age, and grey ellipses are excluded. Data plotted at 95% 658 confidence interval. The uncertainty on the interpreted age is reported as 2σ internal/external. A) 659 Results for hornblende gabbro sample 09AH369A (Geological Survey of Canada laboratory 660 number 10144). Inset: transmitted light images of representative population of zircon grains. B) 661 Results for monzogranite sample 09AH368A (Geological Survey of Canada laboratory number 662 10146). Inset: transmitted light images of representative population of zircon grains. 663 664 Figure 7. A) Mg# in olivine versus NiO wt% content. B) Classification triangle for feldspar. C) 665 Wo-En-Fs ternary diagrams for pyroxene (Morimoto 1988). 666 667 Figure 8. Element, element ratios or trace elements versus Mg# diagrams: A) SiO₂ wt%, B) Co 668 ppm, C) Al₂O₃ wt%, D) Sr/Y, E) Sc ppm; F) CaO/Al₂O₃, G) V/Ti; H) Ti/Zr, and I) Dy/Yb. 669 670 Figure 9. Major-element plots for Silurian magmatism. A) SiO₂ vs. Na₂O/K₂O (Middlemost 671 1994). B) Jensen cation plot (Jensen 1976). C) SiO₂ versus MALI (modified alkali lime index; 672 Na₂O+K₂O-CaO (Frost and Frost 2008). 673 674 Figure 10. Primitive mantle normalized multi-element plot for the Group A samples (A) and 675 chondrite normalized REE diagram (B). Primitive mantle normalized (C) and chondrite 676 normalized diagram (D) for Group B samples. Primitive mantle normalized (E) and chondrite 677 normalized diagram (F) for silicic samples. Normalization values from (Sun and McDonough 678 1989). On all subsequent figures: Normal mid-ocean ridge basalt (N-MORB), enriched mid-679 ocean ridge basalt (E-MORB), and ocean-island basalt (OIB) data from Sun and McDonough 680 (1989). Backarc basin basalt (BAB) from Ewart et al. (1998). Island arc tholeiite (IAT) and calc-681 alkaline basalt (CAB) from Stolz et al. (1990).

- 682 **Figure 11.** A) ¹⁴⁷Sm/¹⁴⁴Nd vs. εNd_(t). B) ⁸⁷Sr/⁸⁶Sr_(i) versus εNd_(t). CHUR chondritic uniform
- reservoir. DM depleted mantle (values calculated according to DePaolo 1988). The field for
- 684 Grenvillian basement rocks from the Long Range Inlier is from Dickin (2004). Mantle array
- inferred at 430 Ma.

687 **Figure 12.** Discrimination diagrams A) La versus La/Sm. B) La versus La/Yb.

688

- Figure 13. A) Zr/Y vs Nb/Y diagram (Fitton et al. 1997). B) Nb/Yb vs Zr/Yb (Pearce and Peate
- 690 1995). C) La_{cn}/Sm_{cn} vs Tb_{cn}/Yb_{cn} (Zhang et al. 2008). D) D) TiO₂/Yb vs. Th/Nb diagram (Pearce
- et al. 2021). The black squares represent average end-member compositions given by Pearce et
- al. (2021). The black double-headed arrow represents a mixing line between IAB and OIB +
- OPB end-member sources. IAB, Island Arc Basalts; OPB, ocean plateau basalts; and SZLM,
- subduction-modified lithospheric mantle. S, subduction component; C, crustal contaminant
- 695 component; W, within plate; f, fractional crystallization; UCC, upper continental crust; BCC,
- 696 bulk continental crust; LCC, lower continental crust. Continental crust values from Taylor and
- 697 McLennan (1995).

698

699

Supplemental Material

- 701 **S1.** Methodology.
- 702 **S2.** Thin sections images of the Taylor Brook Gabbro Suite
- 703 **S3.** U-Pb zircon SHRIMP analytical data.
- 704 **S4**. Cathodoluminescence (CL) images of zircon grains from U-Pb zircon analyses. A)
- Hornblende gabbro (09AH369A; GSC lab number 10144). B) Monzogranite (09AH368A; GSC
- 706 lab number 10146).
- 707 **S5.** Mineral chemical analyses.
- 708 **S6.** Major and trace element geochemical data.
- 709 **S7.** Sr-Nd isotopic data.

711

712

722

723

724

725

726

727

732

733

734

735

736

737738

739

740

741

742

743

744

745

746

References

- Allègre, C.J., and Minster, J.F. 1978. Quantitative models of trace element behavior in magmatic processes. Earth and Planetary Science Letters, **38**: 1-25. doi:10.1016/0012-821X(78)90123-1.
- Annen, C., Blundy, J.D., Leuthold, J., and Sparks, R.S.J. 2015. Construction and evolution of igneous bodies: Towards an integrated perspective of crustal magmatism. LITHOS, **230**: 206-221. doi:10.1016/j.lithos.2015.05.008.
- Barr, S.M., Dehler, S.A., and Zsámboki, L. 2014. Connecting Cape Breton Island and
 Newfoundland, Canada: Geophysical Modeling of pre-Carboniferous 'Basement' Rocks
 in the Cabot Strait Area. Geoscience Canada, 41. doi:10.12789/geocanj.2014.41.041.
 - Black, L.P., Kamo, S.L., Williams, I.S., Mundil, R., Davis, D.W., Korsch, R.J., and Foudoulis, C. 2003. The application of SHRIMP to Phanerozoic geochronology; a critical appraisal of four zircon standards. Chemical Geology, **200**: 171-188. doi:https://doi.org/10.1016/S0009-2541(03)00166-9.
 - Brem, A. 2007. The Late Proterozoic to Palaeozoic Tectonic Evolution of the Long Range Mountains in Southwestern Newfoundland. University of Waterloo.
- Brewer, T.S., Åhäll, K.I., Menuge, J.F., Storey, C.D., and Parrish, R.R. 2004. Mesoproterozoic bimodal volcanism in SW Norway, evidence for recurring pre-Sveconorwegian continental margin tectonism. Precambrian Research, **134**: 249-273. doi:10.1016/j.precamres.2004.06.003.
 - Castonguay, S., Van Staal, C.R., Joyce, N., Skulski, T., and Hibbard, J.P. 2014. Taconic Metamorphism Preserved in the Baie Verte Peninsula, Newfoundland Appalachians: Geochronological Evidence for Ophiolite Obduction and Subduction and Exhumation of the Leading Edge of the Laurentian (Humber) Margin During Closure of the Taconic Seaway. Geoscience Canada, **41**: 459-482. doi:10.12789/geocanj.2014.41.055.
 - Cicconi, M., Rita, Le Losq, C., Henderson, G., S, and Neuville, D., R. 2021. Magma Redox Geochemistry. *In* Magma Redox Geochemistry. Wiley. pp. 381 398.
 - Collins, P.G. 2007. A petrographic and geochemical characterization and the evaluation of the exploration potential for nickel sulfides in several mafic-ultramafic intrusive complexes in Newfoundland. Cambridge.
 - Colman-Sadd, S.P., Hayes, J.P., and Knight, I. 1990. Geology of the Island of Newfoundland. Government of Newfoundland and Labrador, Department of Mines and Energy, Geological Survey Branch, **Map 90-001**.
 - DePaolo, D.J. 1988. Neodymium Isotope Geochemistry. Minerals, Rocks and Mountains. Springer Berlin, Heidelberg.
- Dickin, A.P. 2004. Mesoproterozoic and Paleoproterozoic crustal growth in the eastern Grenville Province: Nd isotope evidence from the Long Range inlier of the Appalachian orogen. Memoir of the Geological Society of America, **197**: 495-503. doi:10.1130/0-8137-1197-5505.
- Dorais, M.J., Marvinney, R.G., and Markert, K. 2017. The age, petrogeneis and tectonic significance of the Frontenac Formation basalts, northern New Hampshire and western Maine. American Journal of Science, **317**: 990-1018. doi:10.2475/09.2017.02.

- Drummond, M.S., and Defant, M.J. 1990. A model for Trondhjemite Tonalite Dacite Genesis and crustal growth via slab melting: Archean to modern comparisons. Journal of Geophysical Research: Solid Earth, **95**: 21503-21521. doi:10.1029/JB095iB13p21503.
- Drummond, M.S., Defant, M.J., and Kepezhinskas, P.K. 1996. Petrogenesis of slab-derived trondhjemite–tonalite–dacite/adakite magmas. Earth and Environmental Science Transactions of The Royal Society of Edinburgh, **87**: 205-215. doi:10.1017/s0263593300006611.
- Dunning, G.R. 1987. U/Pb geochronology of the Coney Head Complex, Newfoundland. Canadian Journal of Earth Sciences, **24**: 1072-1075. doi:10.1139/e87-104.
- Dunning, G.R., O'Brien, S.J., Colman-Sadd, S.P., Blackwood, R.F., Dickson, W.L., O'Neill, P.P., and Krogh, T.E. 1990. Silurian Orogeny in the Newfoundland Appalachians. The Journal of Geology, **98**: 895-913. Available from http://www.jstor.org/stable/30081102 [accessed 2024/12/10/].
 - Erdmer, P. 1986. Geology of the Long Range Inlier in Sandy Lake map area, western Newfoundland. G.S.o. Canada.

768

772

773

774

775

776

777

778

779

780

781

782

783

784 785

786

787

788

- Erdmer, P., and Williams, H. 1995. Grenville basement rocks (Humber Zone). *In* Geology of the
 Appalachian-Caledonian Orogen in Canada and Greenland. Geological Survey of
 Canada. pp. 51-63.
 - Ewart, A., Collerson, K.D., Regelous, M., Wendt, J.I., and Niu, Y. 1998. Geochemical Evolution within the Tonga-Kermadec-Lau Arc-Back-arc Systems: the Role of Varying Mantle Wedge Composition in Space and Time. Journal of Petrology, **39**: 331-368. doi:10.1093/petroj/39.3.331.
 - Fitton, J.G., Saunders, A.D., Norry, M.J., Hardarson, B.S., and Taylor, R.N. 1997. Thermal and chemical structure of the Iceland plume. Earth and Planetary Science Letters, **153**: 197-208. doi:10.1016/S0012-821X(97)00170-2.
 - Frost, B.R., and Frost, C.D. 2008. A geochemical classification for feldspathic igneous rocks. Journal of Petrology, **49**: 1955-1969. doi:10.1093/petrology/egn054.
 - Goldstein, S.L., O'Nions, R.K., and Hamilton, P.J. 1984. A Sm-Nd isotopic study of atmospheric dusts and particulates from major river systems. Earth and Planetary Science Letters, **70**: 221-236. doi:10.1016/0012-821X(84)90007-4.
 - Guillaume, B., Gianni, G.M., Kermarrec, J.-J., and Bock, K. 2022. Control of crustal strength, tectonic inheritance, and stretching/ shortening rates on crustal deformation and basin reactivation: insights from laboratory models. Solid Earth, **13**: 1393-1414. doi:10.5194/se-13-1393-2022.
 - Hatcher, R.D. 2010. The Appalachian orogen: A brief summary. Memoir of the Geological Society of America, **206**: 1-19. doi:10.1130/2010.1206(01).
- 790 Heaman, L.M., and LeCheminant, A.N. 1993. Paragenesis and U-Pb systematics of baddeleyite 791 (ZrO2). Chemical Geology, **110**: 95-126. doi:https://doi.org/10.1016/0009-2541(93)90249-I.
- Heaman, L.M., Bowins, R., and Crocket, J. 1990. The chemical composition of igneous zircon suites: implications for geochemical tracer studies. Geochimica et Cosmochimica Acta, 54: 1597-1607. doi:https://doi.org/10.1016/0016-7037(90)90394-Z.
- Heaman, L.M., Erdmer, P., and Owen, J.V. 2002. U–Pb geochronologic constraints on the
 crustal evolution of the Long Range Inlier, Newfoundland. Canadian Journal of Earth
 Sciences, 39: 845-865. doi:10.1139/e02-015.

- Hinchey, A.M. 2010. Geology of the Northern Portion of the Silver Mountain Map area (NTS 12H/11), Southern Long Range Inlier, Newfoundland. Current Research (2010)
 Newfoundland and Labrador Department of Natural Resources Geological Survey,
 Report 10-1: 245-263. doi:10.13140/RG.2.2.18689.07520.
- Hinchey, A.M. 2020. Geology of the Northern Silver Mountain Map Area (NTS 12H/11). Scale 1:50 000. Newfoundland and Labrador, Department of Industry, Energy and Technology, Geological Survey, Map 2020-18, Open File, **12H/11**: 1. doi:10.13140/RG.2.2.18689.07520.
- Hinchey, A.M., Knight, I., Sandeman, H.A., and Hinchey, J.G. 2022. Tournaisian volcanism associated with transtensional basin development in western Newfoundland during the amalgamation of Pangea. Gondwana Research, **110**: 226-248. doi:10.1016/j.gr.2022.06.013.
- Hinchey, A.M., Serna Ortiz, S., Skipton, D., and Mendoza Marin, D. 2025. Metasedimentary sequences in the Long Range Inlier: Detrital zircon evidence for post-Grenvillian sedimentary deposition. Current Research (2025), Newfoundland and Labrador Department of Industry, Energy and Technology, Geological Survey, Report, **25-1**: 115-130. doi:10.13140/RG.2.2.25937.03683.
- Holder, R.M., Yakymchuk, C., and Viete, D.R. 2020. Accessory Mineral Eu Anomalies in
 Suprasolidus Rocks: Beyond Feldspar. Geochemistry, Geophysics, Geosystems, 21.
 doi:10.1029/2020gc009052.
- Honsberger, I.W., Bleeker, W., Kamo, S.L., Sandeman, H.A.I., Evans, D.T.W., Rogers, N., van Staal, C.R., and Dunning, G.R. 2022. Latest Silurian syntectonic sedimentation and magmatism and Early Devonian orogenic gold mineralization, central Newfoundland Appalachians, Canada: Setting, structure, lithogeochemistry, and high-precision U-Pb geochronology. GSA Bulletin, **134**: 2933-2957. doi:10.1130/b36083.1.
- Hyde, R.S., Miller, H.G., Hiscott, R.N., and Wright, J.A. 2007. Basin architecture and thermal maturation in the strike slip Deer Lake Basin, Carboniferous of Newfoundland. Basin Research, 1: 85-105. doi:10.1111/j.1365-2117.1988.tb00007.x.
- Jensen, L.S. 1976. A new cation plot for classifying subalkalic volcanic rocks. Ontario Division Mines, Miscellaneous Paper,, **66**: 22.
- Kamo, S.L., Gower, C.F., Kamo[^], S.L., and Gower[^], C.F. 1994. Note: U-Pb baddeleyite dating clarifies age of characteristic paleomagnetic remanence of Long Range dykes, southeastern Labrador. Atlantic Geology, **30**: 259-262.
 - Karabinos, P., Morris, D., Hamilton, M., and Rayner, N. 2008. Age, origin, and tectonic significance of Mesoproterozoic and Silurian felsic sills in the Berkshire massif, Massachusetts. American Journal of Science, **308**: 787-812. doi:10.2475/06.2008.03.

- Lissenberg, C.J., McNicoll, V.J., and van Staal, C.R. 2006. The origin of mafic-ultramafic bodies within the northern Dashwoods subzone, Newfoundland Appalachians. Atlantic Geology, 42: 1-12. doi:10.4138/2152.
- Ludwig, K. 2012. User's manual for Isoplot/Ex rev. 3.70: a Geochronological Toolkit for Microsoft Excel. *In* Special Publication. Special Publication 5, Berkeley Geochronology Center, Berkeley, Berkeley, pp. 1-76.
- Matton, G., and Jébrak, M. 2009. The Cretaceous Peri-Atlantic Alkaline Pulse (PAAP): Deep mantle plume origin or shallow lithospheric break-up? Tectonophysics, **469**: 1-12. doi:10.1016/j.tecto.2009.01.001.

- Menuge, J.F., Brewer, T.S., and Seeger, C.M. 2002. Petrogenesis of metaluminous A-type rhyolites from the St Francois Mountains, Missouri and the Mesoproterozoic evolution of the southern Laurentian margin. Precambrian Research, **113**: 269-291. doi:10.1016/s0301-9268(01)00211-x.
- Middlemost, E.A.K. 1994. Naming materials in the magma/igneous rock system. Earth-Science Reviews, **37**: 215-224. doi:https://doi.org/10.1016/0012-8252(94)90029-9.
- Morimoto, N. 1988. Nomenclature of Pyroxenes. Mineralogy and Petrology, **39**: 55-76. doi:10.1007/BF01226262.
- Morris, J.D., and Ryan, J.G. 2003. Subduction Zone Processes and Implications for Changing
 Composition of the Upper and Lower Mantle. *In* Treatise on Geochemistry. Elsevier. pp.
 451-470.
- Moyen, J.-F., Janoušek, V., Laurent, O., Bachmann, O., Jacob, J.-B., Farina, F., Fiannacca, P., and Villaros, A. 2021. Crustal melting vs. fractionation of basaltic magmas: Part 1, granites and paradigms. LITHOS, **402-403**: 106291. doi:10.1016/j.lithos.2021.106291.
- Müntener, O., Kelemen, P.B., and Grove, T.L. 2001. The role of H2O during crystallization of primitive arc magmas under uppermost mantle conditions and genesis of igneous pyroxenites: An experimental study. Contributions to Mineralogy and Petrology, **141**: 643-658. doi:10.1007/s004100100266.

863

864865

866

867

868

869

870

871

872

873

874

875

876

877

878

- Murphy, J.B. 2003. Late Palaeozoic formation and development of the St Marys Basin, mainland Nova Scotia, Canada: a prolonged record of intracontinental strike-slip deformation during the assembly of Pangaea. Geological Society, London, Special Publications, **210**: 185-196. doi:10.1144/gsl.Sp.2003.210.01.11.
- Murphy, J.B., van Staal, C.R., and Duncan Keppie, J. 1999. Middle to late Paleozoic Acadian orogeny in the northern Appalachians: A Laramide-style plume-modified orogeny? Geology, **27**: 653-656. doi:10.1130/0091-7613(1999)027<0653:Mtlpao>2.3.Co;2.
- Murphy, J.B., Keppie, J.D., Nance, R.D., and Dostal, J. 2010. Comparative evolution of the Iapetus and Rheic Oceans: A North America perspective. Gondwana Research, 17: 482-499. doi:10.1016/j.gr.2009.08.009.
- Owen, J.V. 1991. Geology of the Long Range Inlier, Newfoundland. *In* Geological Survey of Canada, Bulletin 395. Geological Survey of Canada, Bulletin 395. p. 89.
- Pearce, J.A., and Peate, D.W. 1995. Tectonic Implications of the Composition of Volcanic ARC Magmas. Annual Review of Earth and Planetary Sciences, **23**: 251-285. doi:10.1146/annurev.ea.23.050195.001343.
- Pirajno, F. 2010. Intracontinental strike-slip faults, associated magmatism, mineral systems and mantle dynamics: examples from NW China and Altay-Sayan (Siberia). Journal of Geodynamics, **50**: 325-346. doi:10.1016/j.jog.2010.01.018.
- Rankin, D.W., Coish, R.A., Tucker, R.D., Peng, Z.X., Wilson, S.A., and Rouff, A.A. 2007.
 Silurian extension in the Upper Connecticut Valley, United States and the origin of middle Paleozoic basins in the Québec embayment. American Journal of Science, 307: 216-264. doi:10.2475/01.2007.07.
- Rocchi, S., Storti, F., Di Vincenzo, G., and Rossetti, F. 2003. Intraplate strike-slip tectonics as an alternative to mantle plume activity for the Cenozoic rift magmatism in the Ross Sea region, Antarctica. Geological Society, London, Special Publications, **210**: 145-158. doi:10.1144/gsl.Sp.2003.210.01.09.
- Rudnick, R.L., and Gao, S. 2003. Composition of the Continental Crust. Treatise on Geochemistry, **3-9**: 1-64. doi:10.1016/B0-08-043751-6/03016-4.

- Saccani, E., Azimzadeh, Z., Dilek, Y., and Jahangiri, A. 2013. Geochronology and petrology of the Early Carboniferous Misho Mafic Complex (NW Iran), and implications for the melt evolution of Paleo-Tethyan rifting in Western Cimmeria. LITHOS, **162-163**: 264-278. doi:10.1016/j.lithos.2013.01.008.
- Sandeman, H.A.I., and Dunning, G.R. 2016. Preliminary U–Pb geochronology and petrochemistry of volcanic rocks and felsic dykes of the Silurian Sops Arm Group, White Bay, western Newfoundland (NTS 2H/10 and 15). Current Research, Newfoundland and Labrador Department of Natural Resources Geological Survey, **Report 16-1**: 39-69. doi:10.13140/RG.2.1.2380.2642.
- Sandeman, H.A.I., Honsberger, I.W., Peddle, C., Kamo, S.L., and Dunning, G.R. 2024.

 Petrochemical and geochronological constraints on the origin of the Sops Arm group, the most westerly Silurian volcano-sedimentary extensional basin on the western Newfoundland composite Laurentian margin. Canadian Journal of Earth Sciences.

 doi:10.1139/cjes-2024-0032.
- 904 Smyth, W.R., and Schillereff, H.S. 1982. The Pre-Carboniferous geology of southwest White
 905 Bay. Current Research, Government of Newfoundland and Labrador, Department of
 906 Mines and Energy, Mineral Development Division, Report 82-01, Current Research,
 907 Government of Newfoundland and Labrador, Department of Mines and Energy, Mineral
 908 Development Division, Report 82-01,
- Stockmal, G.S., Colman Sadd, S.P., Keen, C.E., Marillier, F., O'Brien, S.J., and Quinlan, G.M.
 1990. Deep seismic structure and plate tectonic evolution of the Canadian Appalachians.
 Tectonics, 9: 45-62. doi:10.1029/TC009i001p00045.
- 912 Stolz, A.J., Varne, R., Davies, G.R., Wheller, G.E., and Foden, J.D. 1990. Magma source 913 components in an arc-continent collision zone: the Flores-Lembata sector, Sunda arc, 914 Indonesia. Contributions to Mineralogy and Petrology, **105**: 585-601. 915 doi:10.1007/BF00302497.
 - Sun, S.-s., and McDonough, W.F. 1989. Chemical and isotopic systematics of oceanic basalts: implications for mantle composition and processes. Geological Society, London, Special Publications, 42: 313-345. doi:10.1144/GSL.SP.1989.042.01.19.
 - Taylor, S.R., and McLennan, S.M. 1995. The geochemical evolution of the continental crust. Reviews of Geophysics, **33**: 241. doi:10.1029/95RG00262.
- Terakado, Y., and Fujitani, T. 1995. Significance of iron and cobalt partitioning between plagioclase and biotite for problems concerning the Eu2+/Eu3+ ratio, europium anomaly, and magnetite-/ilmenite-series designation for granitic rocks from the Inner Zone of southwestern Japan. Geochimica et Cosmochimica Acta, **59**: 2689-2699. doi:https://doi.org/10.1016/0016-7037(95)00165-V.
- 926 Thomas, W.A. 2006. Tectonic inheritance at a continental margin. GSA Today, **16**. doi:10.1130/1052-5173(2006)016[4:Tiaacm]2.0.Co;2.

917

918

919

- van der Velden, A.J., van Staal, C.R., and Cook, F.A. 2004. Crustal structure, fossil subduction,
 and the tectonic evolution of the Newfoundland Appalachians: Evidence from a
 reprocessed seismic reflection survey. Geological Society of America Bulletin, 116:
 1485-1498. doi:10.1130/B25518.1.
- van Staal, C.R., and Barr, S.M. 2012. Lithospheric architecture and tectonic evolution of the
 Canadian Appalachians and associated Atlantic margin. *In* Tectonic Styles in Canada:
 The LITHOPROBE Perspective. *Edited by* J.A. Percival and F.A. Cook and R.M.
- 935 Clowes. Geological Association of Canada, Special Paper 49. pp. 41-95.

van Staal, C.R., and Zagorevski, A. 2022. Paleozoic tectonic evolution of the rifted margins of
 Laurentia. *In* Laurentia: Turning Points in the Evolution of a Continent. Geological
 Society of America.

- van Staal, C.R., Zagorevski, A., McNicoll, V.J., and Rogers, N. 2014. Time-Transgressive Salinic and Acadian Orogenesis, Magmatism and Old Red Sandstone Sedimentation in Newfoundland. Geoscience Canada, **41**: 138-164. doi:10.12789/geocanj.2014.41.031.
 - van Staal, C.R., Barr, S.M., Waldron, J.W.F., Schofield, D.I., Zagorevski, A., and White, C.E. 2021. Provenance and Paleozoic tectonic evolution of Ganderia and its relationships with Avalonia and Megumia in the Appalachian-Caledonide orogen. Gondwana Research, **98**: 212-243. doi:10.1016/j.gr.2021.05.025.
- van Staal, C.R., Lin, S., Valverde-Vaquero, P., Dunning, G., Burgess, J., Schofield, D., and Joyce, N. 2024. Tectonic evolution of high-grade metamorphic tectonites of the Meelpaeg structure near Port aux Basques, southwestern Newfoundland during the Silurian Salinic and Early-to-Middle Devonian Acadian orogenies. Canadian Journal of Earth Sciences. doi:10.1139/cjes-2023-0141.
- Waldron, J.W.F., and Stockmal, G.S. 1994. Structural and tectonic evolution of the Humber Zone, western Newfoundland 2. A regional model for Acadian thrust tectonics. Tectonics, **13**: 1498-1513. doi:10.1029/94tc01505.
- Waldron, J.W.F., Barr, S.M., Park, A.F., White, C.E., and Hibbard, J. 2015. Late Paleozoic strike-slip faults in Maritime Canada and their role in the reconfiguration of the northern Appalachian orogen. Tectonics, **34**: 1661-1684. doi:10.1002/2015tc003882.
- Waldron, J.W.F., McCausland, P.J.A., Barr, S.M., Schofield, D.I., Reusch, D., and Wu, L. 2022. Terrane history of the Iapetus Ocean as preserved in the northern Appalachians and western Caledonides. Earth-Science Reviews, **233**. doi:10.1016/j.earscirev.2022.104163.
- Wang, C., Wang, T., van Staal, C.R., Hou, Z., and Lin, S. 2024. Evolution of Silurian to Devonian magmatism associated with the Acadian orogenic cycle in eastern and southern Newfoundland Appalachians: Evidence for a three-stage evolution characterized by episodic hinterland- and foreland-directed migration of granitoid magmatism. Geological Society of America Bulletin, **136**: 4648-4670. doi:10.1130/b37336.1.
- Whalen, J.B., Rogers, N., van Staal, C.R., Longstaffe, F.J., Jenner, G.A., and Winchester, J.A. 1998. Geochemical and isotopic (Nd, O) data from Ordovician felsic plutonic and volcanic rocks of the Miramichi Highlands: petrogenetic and metallogenic implications for the Bathurst Mining Camp. Canadian Journal of Earth Sciences, **35**: 237-252. doi:10.1139/e97-102.
- Whalen, J.B., McNicoll, V.J., van Staal, C.R., Lissenberg, C.J., Longstaffe, F.J., Jenner, G.A., and van Breeman, O. 2006. Spatial, temporal and geochemical characteristics of Silurian collision-zone magmatism, Newfoundland Appalachians: An example of a rapidly evolving magmatic system related to slab break-off. LITHOS, **89**: 377-404. doi:10.1016/j.lithos.2005.12.011.
- White, L.T., and Ireland, T.R. 2012. High-uranium matrix effect in zircon and its implications for SHRIMP U–Pb age determinations. Chemical Geology, 306-307: 78-91.
 doi:https://doi.org/10.1016/j.chemgeo.2012.02.025.
- Williams, H. 1995. Geology of the Appalachian-Caledonian Orogen in Canada and Greenland.
 Geological Society of America, London.
- 980 Wilson, R.A., van Staal, C.R., and Kamo, S.L. 2017. Rapid transition from the salinic to Acadian 981 orogenic cycles in the northern Appalachian Orogen: Evidence from northern New

982	Brunswick, Canada. American Journal of Science, 317: 449-482.
983	doi:10.2475/04.2017.02.
984	Yule, C.T.G., and Spandler, C. 2022. Geophysical and Geochemical Evidence for a New Mafic
985	Magmatic Province Within the Northwest Shelf of Australia. Geochemistry, Geophysics,
986	Geosystems, 23. doi:10.1029/2021gc010030.
987	Zamboni, D., Gazel, E., Ryan, J.G., Cannatelli, C., Lucchi, F., Atlas, Z.D., Trela, J., Mazza, S.E.,
988	and De Vivo, B. 2016. Contrasting sediment melt and fluid signatures for magma
989	components in the Aeolian Arc: Implications for numerical modeling of subduction
990	systems. Geochemistry, Geophysics, Geosystems, 17: 2034-2053.
991	doi:10.1002/2016GC006301.
992	Zhang, X., Zhang, H., Tang, Y., Wilde, S.A., and Hu, Z. 2008. Geochemistry of Permian
993	bimodal volcanic rocks from central Inner Mongolia, North China: Implication for
994	tectonic setting and Phanerozoic continental growth in Central Asian Orogenic Belt.
995	Chemical Geology, 249 : 262-281. doi:10.1016/j.chemgeo.2008.01.005.
996	

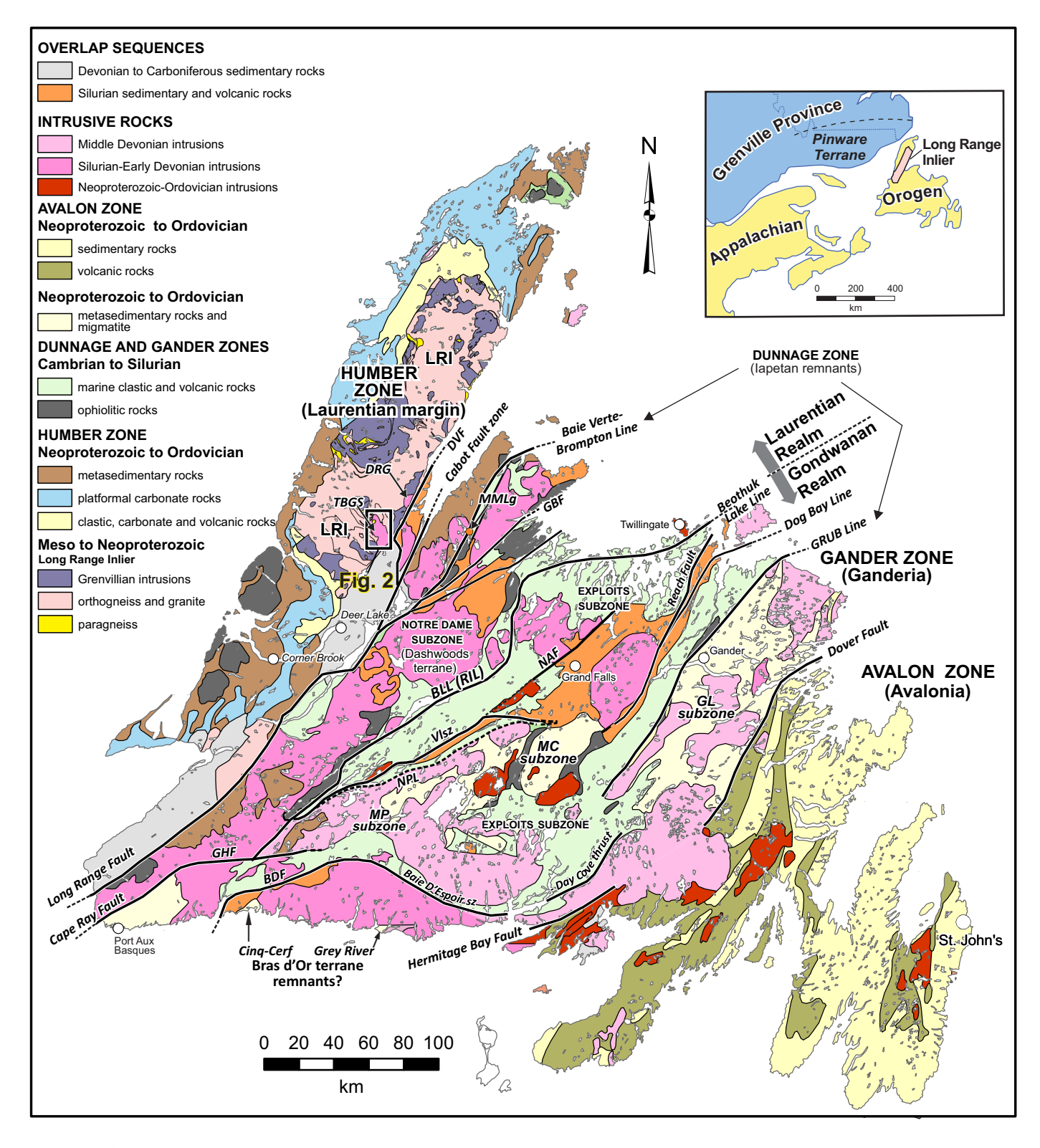


Figure 1

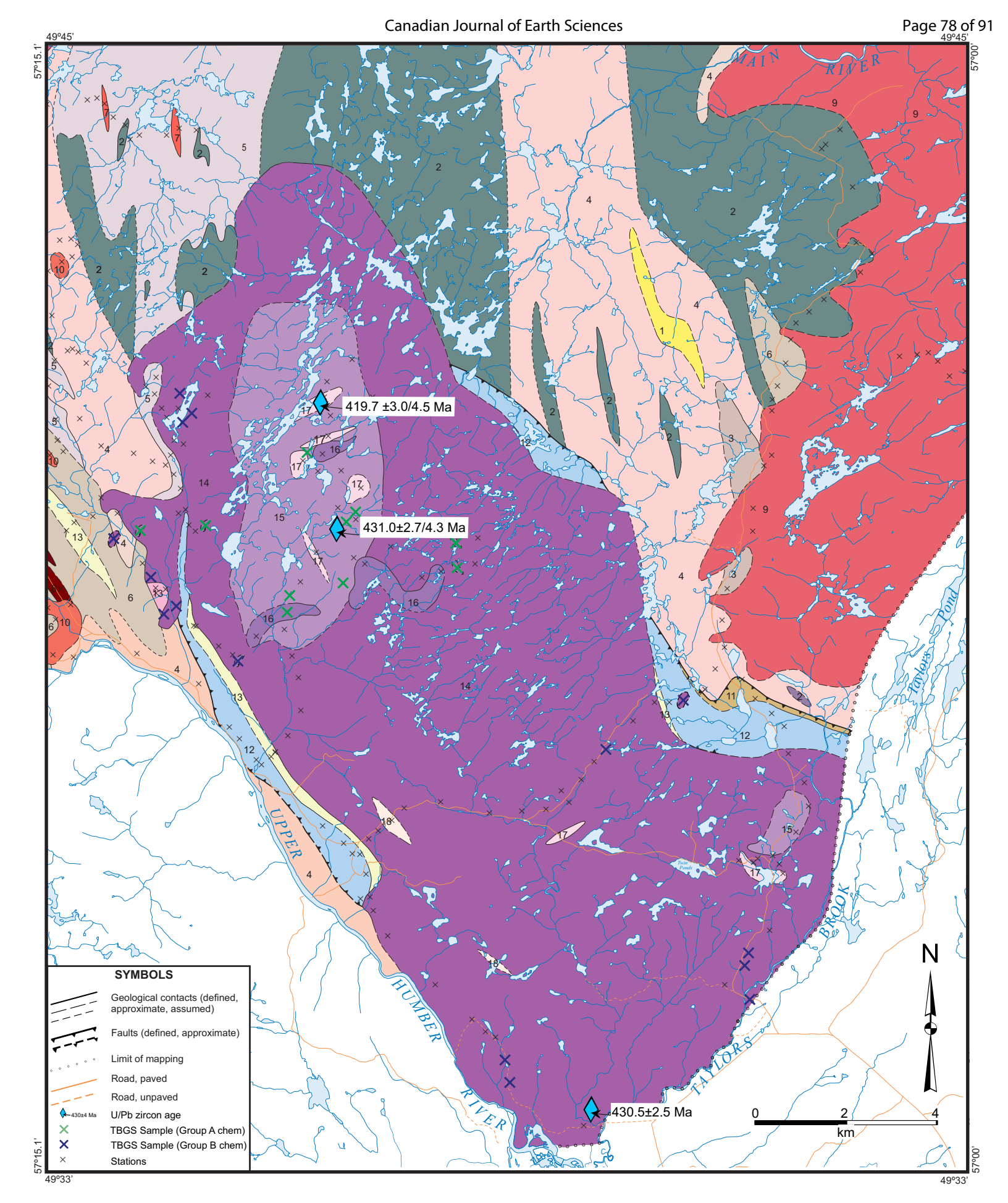


Figure 2

LEGEND

EARLY SILURIAN

- 18 Quartz–feldspar–porphyry rhyolite
- 17 Biotite monzogranite

Taylor Brook Gabbro Suite

- 16 Olivine gabbro to gabbronorite
- Pegmatitic hornblende gabbro to gabbronorite tomelanogabbro
- Gabbro with minor gabbronorite, melanogabbro, and norite

LATE NEOPROTEROZOIC TO ORDOVICIAN

- 13 Semi-pelitic gneiss and quartzite
- 12 Marble to, locally, dolomite
- 11 Phyllite to pelitic schist

LATE MESOPROTEROZOIC TO NEOPROTEROZOIC

10 Hornblende metagabbro

GRENVILLIAN PLUTONIC ROCKS (~1056–970 Ma)

Main River Pluton

9 Biotite <u>+</u> hornblende monzogranite to quartz monzonite

Unnamed Intrusions

- Biotite <u>+</u> hornblende metaquartz monzonite to metamonzogranite
- 7 Biotite-hornblende metagabbro

LATE PALEOPROTEROZOIC TO EARLY MESOPROTERZOIC LONG RANGE GNEISS COMPLEX

Orthogneiss

- Biotite hornblende <u>+</u> orthopyroxene metagranodiorite to metadiorite
- 5 Orthopyroxene–biotite metatonalite to metagranodiorite
- Biotite <u>+</u> hornblende <u>+</u> orthopyroxene monzogranitic to granodioritic gneiss
- Moderately foliated to locally gneissic metadiorite to metaquartz diorite
- 2 Amphibolite

Paragneiss

1 Interlayered quartzite and quartz-rich paragneiss

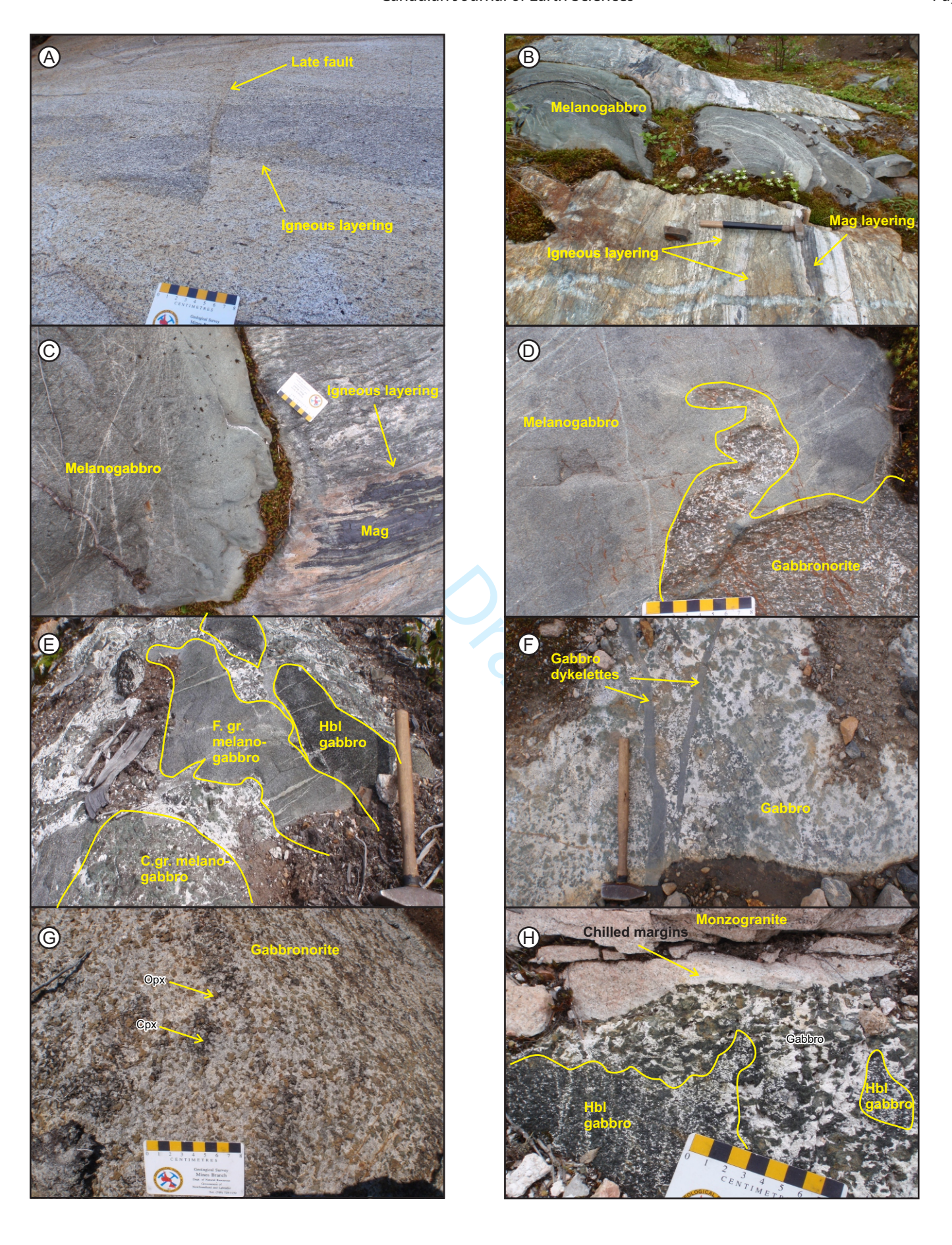
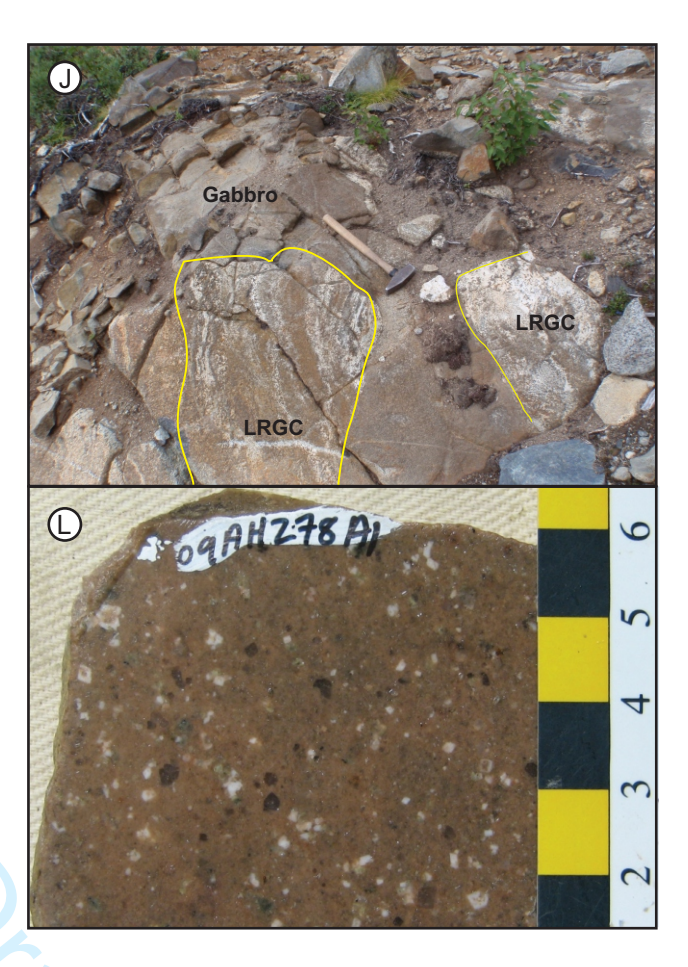
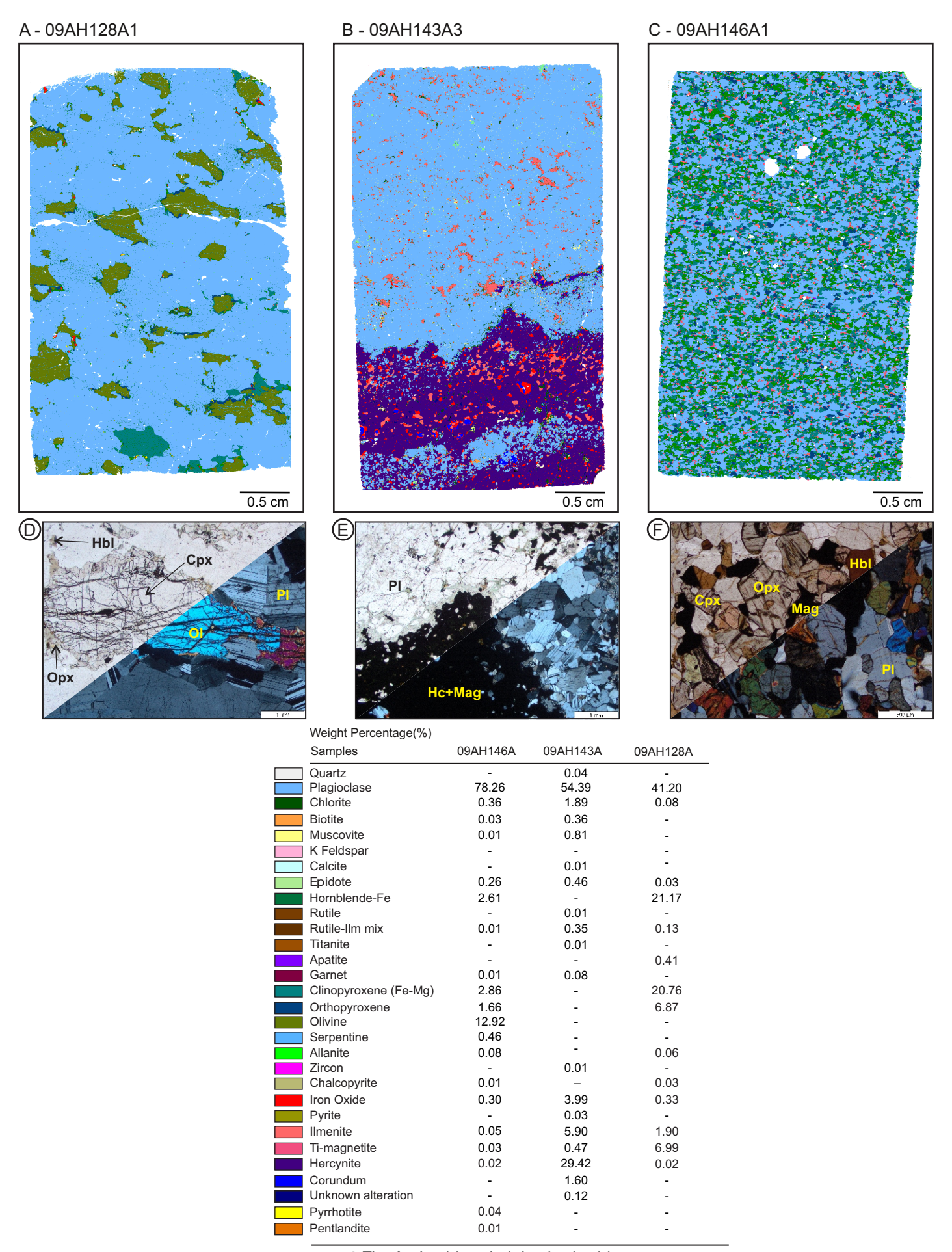


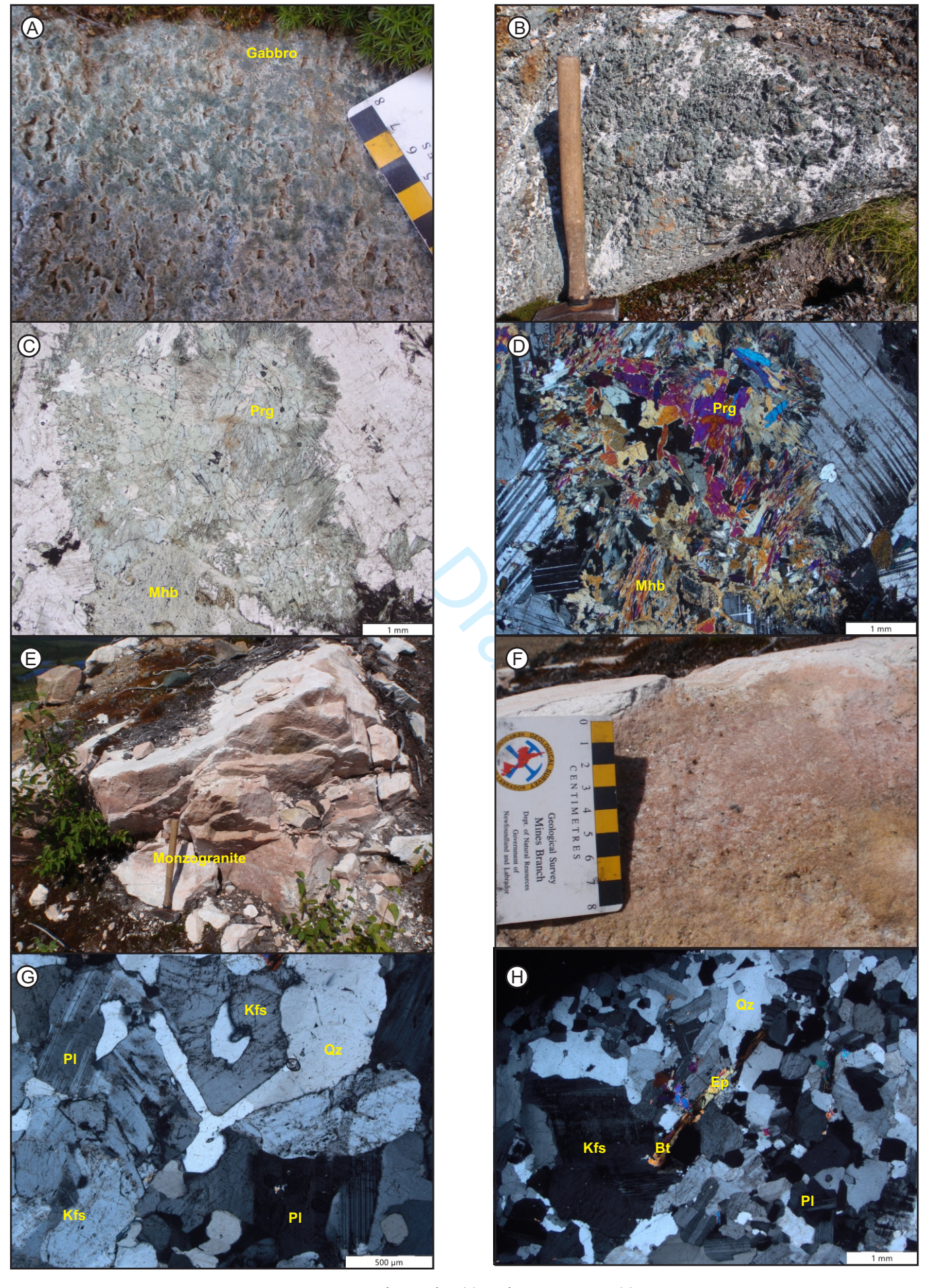
Figure 3



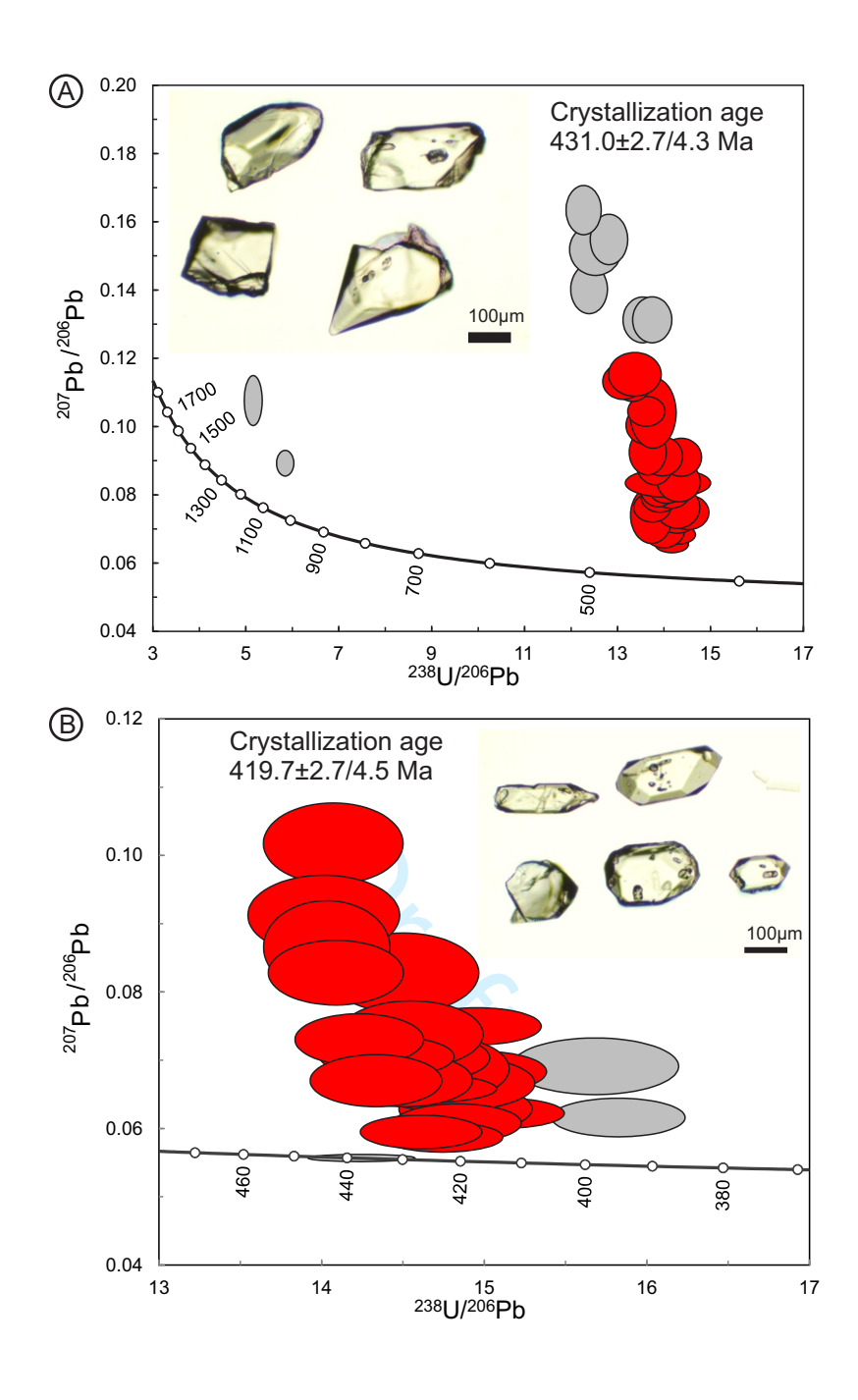


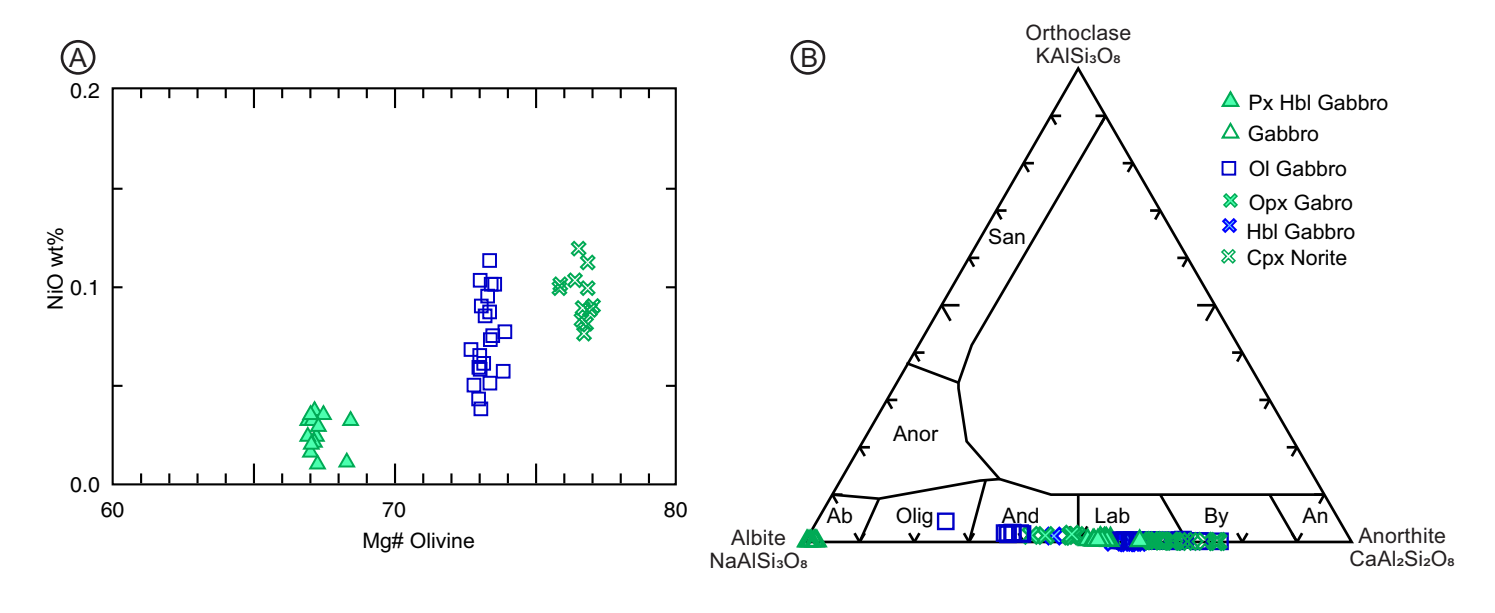


© The Author(s) or their Institution(s)



© The Author(s) or their Institution(s)





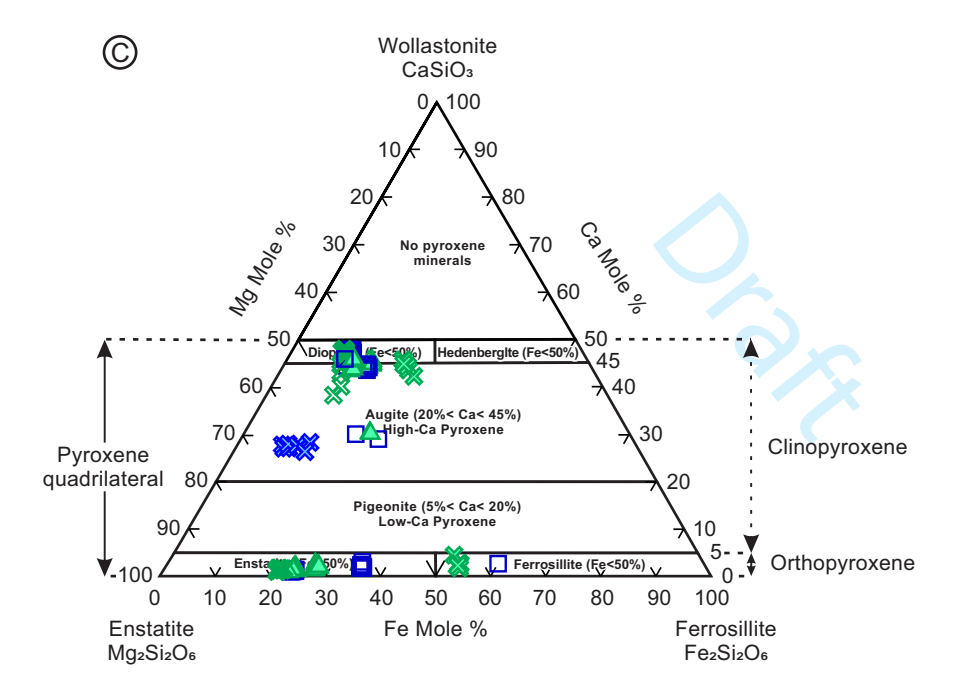
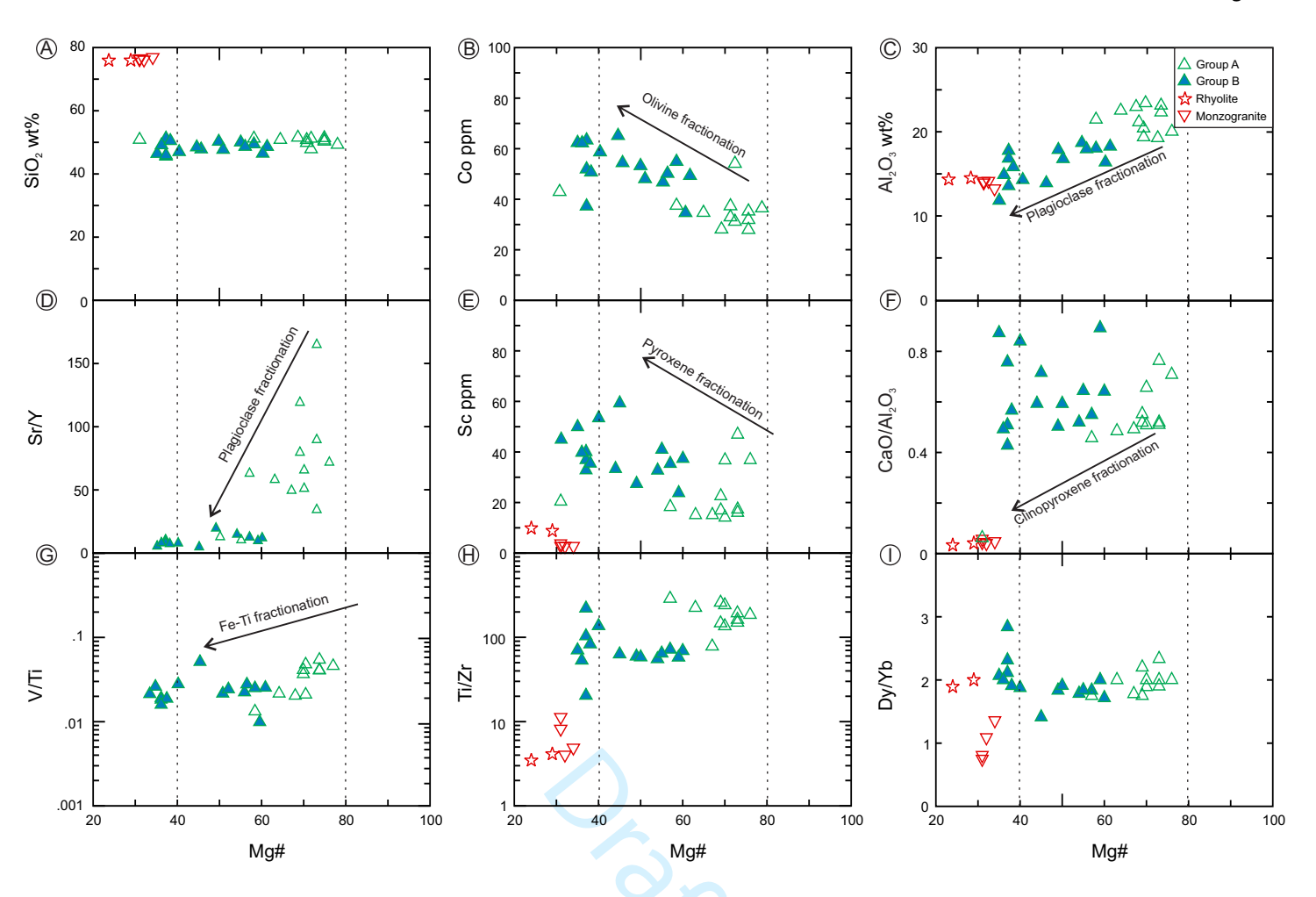


Figure 7



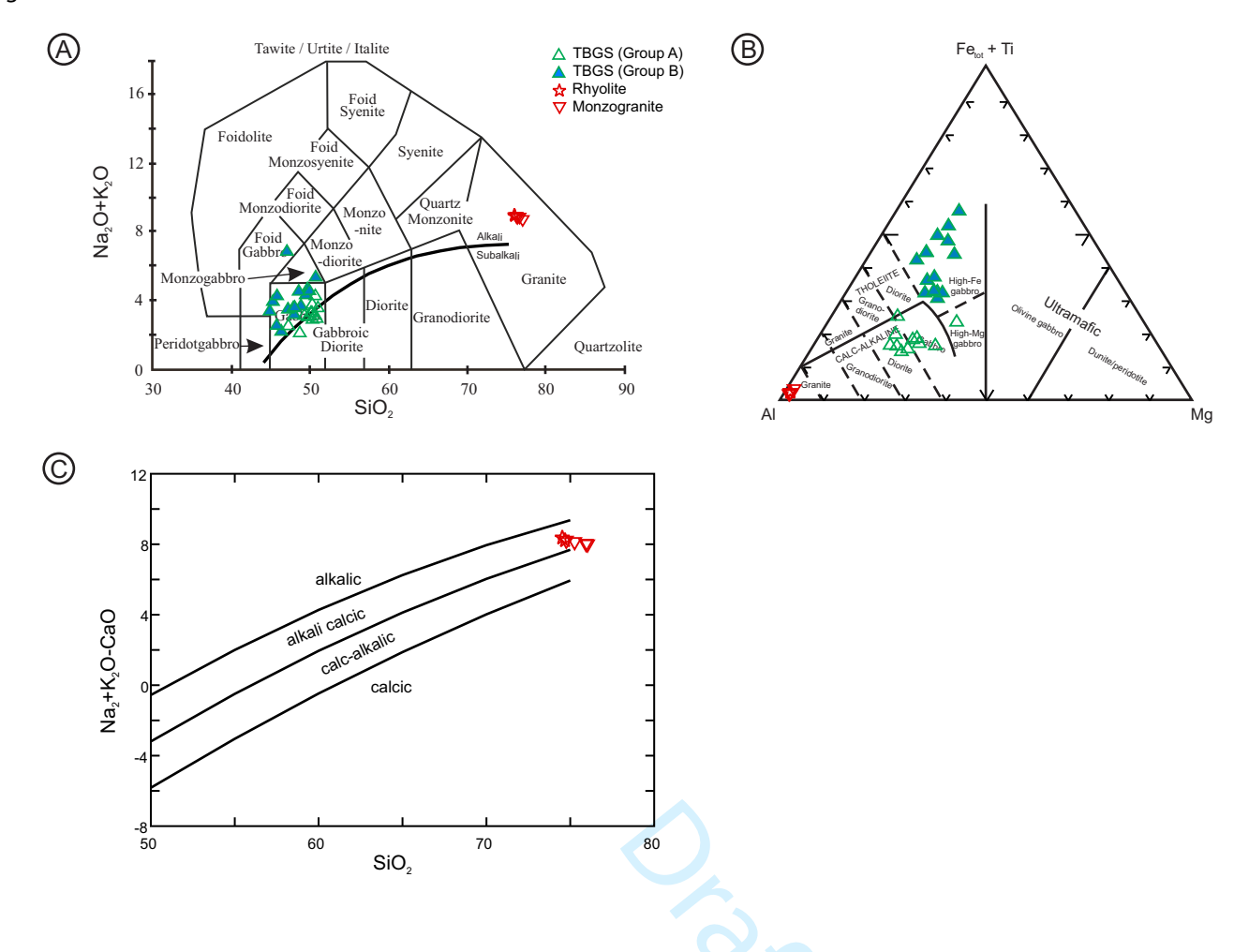
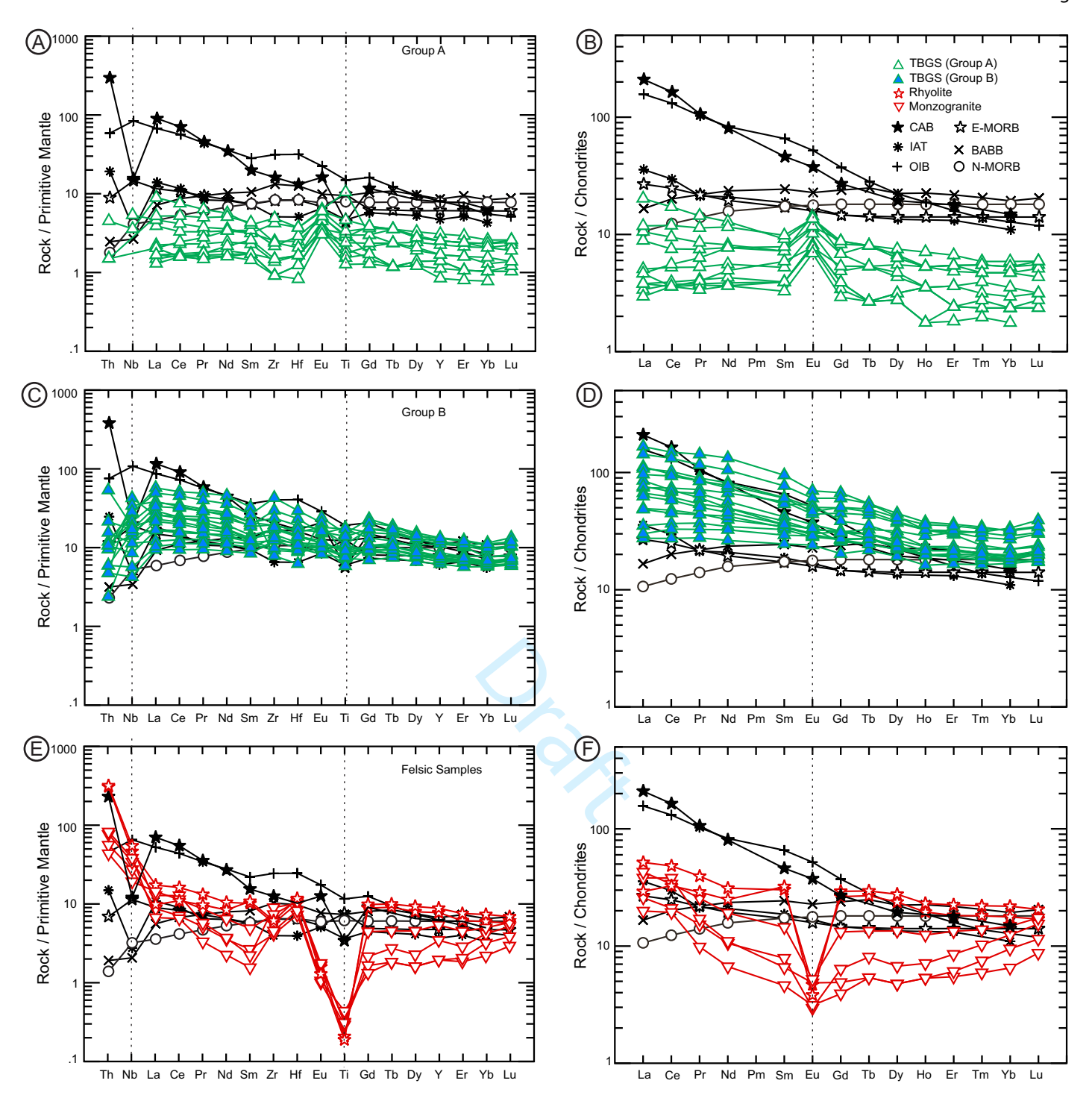
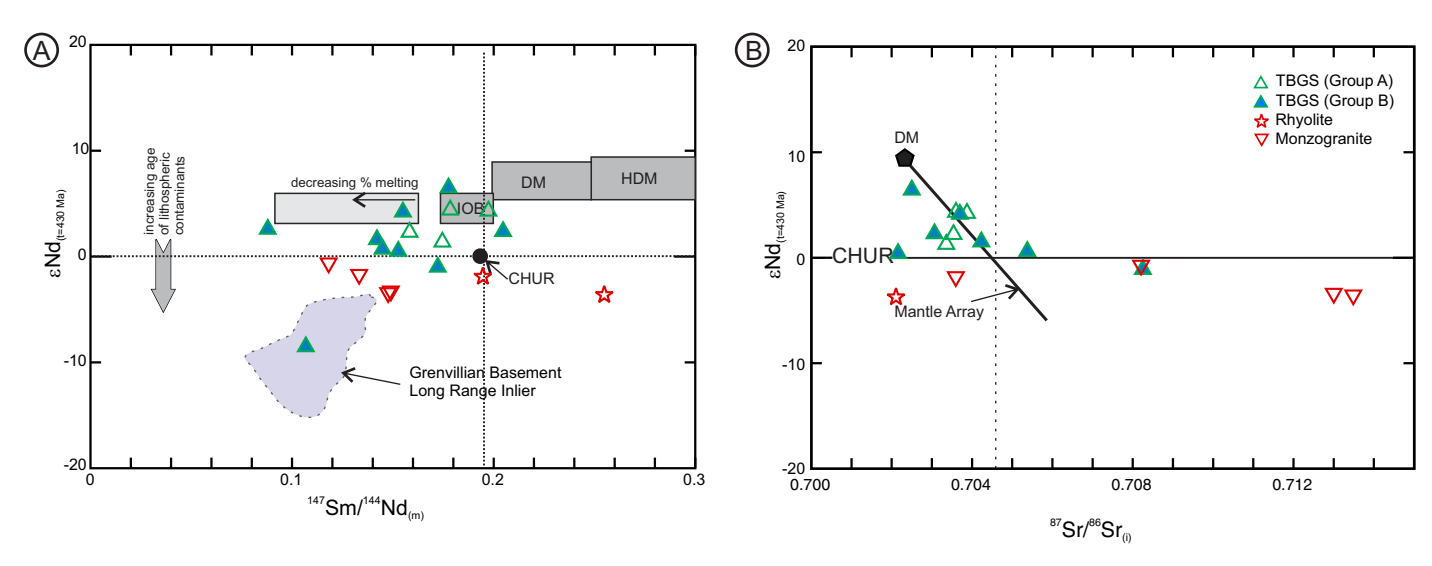
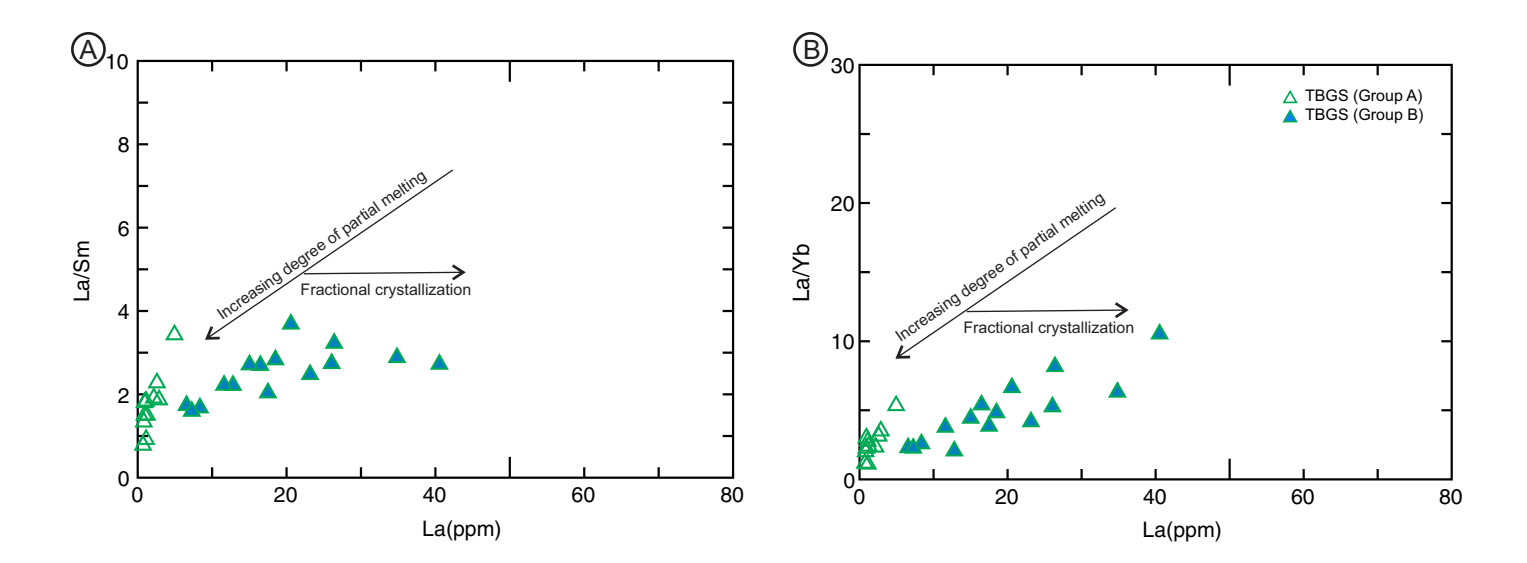


Figure 9











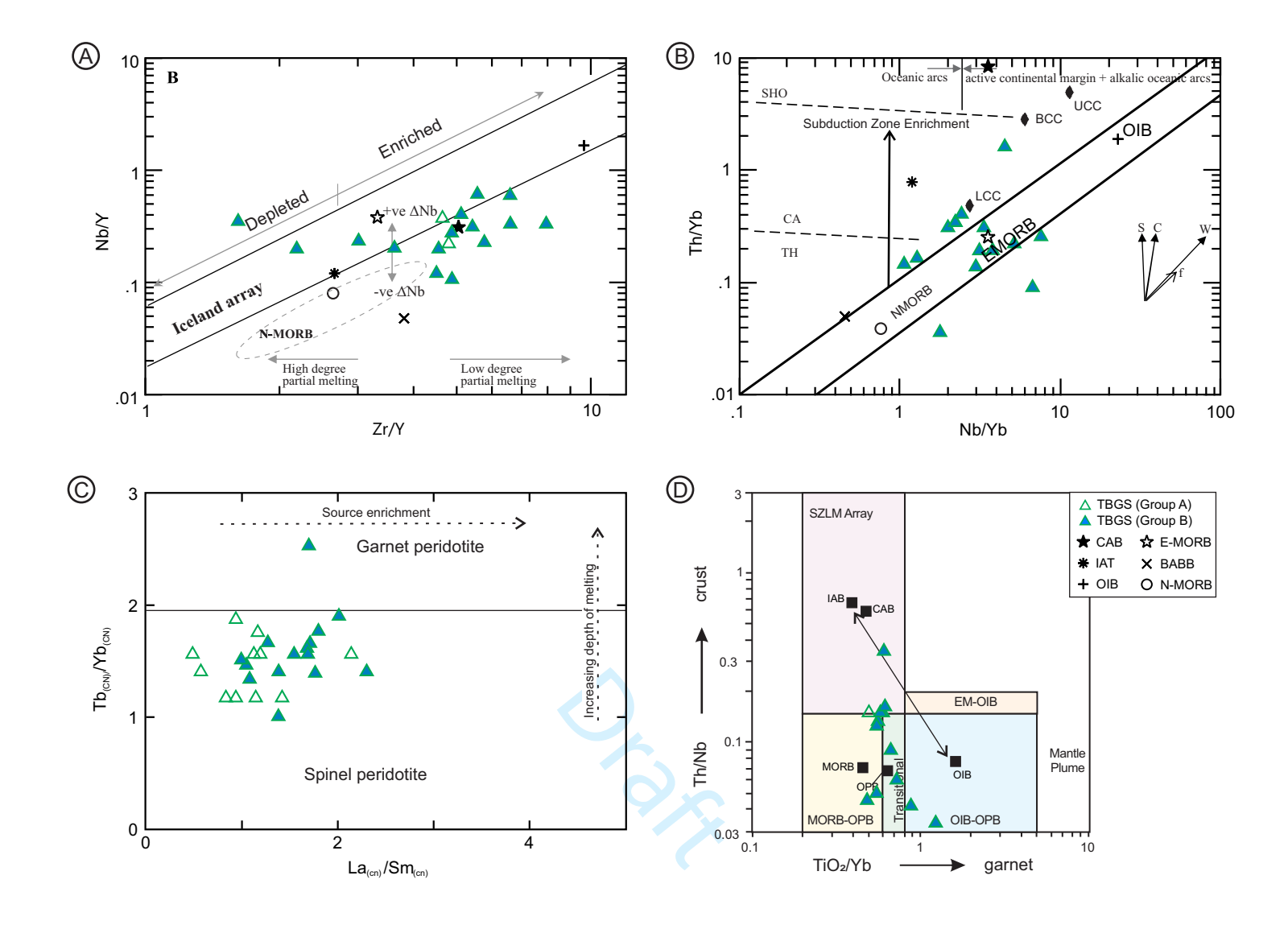


Figure 13

Supplemental Material S1

Silurian mafic magmatism related to post-collisional extension, Appalachian orogen, western Newfoundland

A.M. Hinchey^{1*}, J.G. Hinchey¹, H.A. Sandeman¹, C.J. Lissenberg², N. Rayner³ and Daniela Mendoza Marin¹

Methodology

1. Fieldwork and Petrology

Bedrock mapping (1:50,000) and sampling were undertaken in the Silver Mountain Map Area (NTS 12H/11) during the field seasons of 2009 and 2010 (Hinchey 2010). A map was subsequently released in 2020 (Hinchey 2020). Representative samples of all units were examined petrographically. Diagnostic lithological aspects, such as structures, textures (i.e. grain size), type and modal abundances of constituent minerals were determined by petrography of over 300 thin sections and associated rock slabs were stained for potassium feldspar abundances.

2. U-Pb Geochronology

Zircon from each sample reported herein was imaged using a scanning electron microscope before U-Pb isotopic analysis using the sensitive high-resolution ion microprobe (SHRIMP). Sample locations are illustrated in Figure 3. Analytical data is reported in Supplemental Material S3.

Field samples were reduced in size with a crusher and a disk mill, followed by density separation using a Wilfley table and heavy liquids, from which zircon separates were isolated by hand panning the heavy minerals at Memorial University in Newfoundland. The subsequent imagery and analysis was completed at the Geological Survey of Canada, Ottawa. For Sensitive-High-Resolution-Ion-Microprobe (SHRIMP) analysis selected grains were cast in epoxy mounts.

The minerals were exposed through polishing with a diamond compound, and internal features were characterized in back-scattered electron mode (BSE) and cathodoluminescence (CL) modes utilizing a scanning electron microscope. Mount surfaces were evaporatively coated with 10 nm of high-purity Au.

SHRIMP analytical procedures followed those described by (Stern 1997). Fragments of primary zircon reference material (RM) 6266 (206Pb/238U age = 559±0.2 Ma, (Stern and Amelin 2003) were analyzed on the same mount and under the same conditions as the unknowns. Analyses were conducted using an O- primary beam, with a 20 µm diameter spot with a beam current between 4-10 nA. The count rates of the isotopes of U, Th, and Pb as well as Hf and Yb for zircon were sequentially measured over six scans with a single electron multiplier. Off-line data processing was accomplished using Squid2.5 (Ludwig 2009). Decay constants used follow the recommendations of Steiger and Jäger (1977). The 1σ external errors of $^{206}\text{Pb}/^{238}\text{U}$ ratios reported in the data table incorporate a $\pm 0.9\%$ uncertainty in calibrating the primary RM (Stern and Amelin 2003). Details of the analytical session (mount/session number, spot size, primary beam intensity) are recorded in the footnotes of the data table (Supplementary Material S3) as is the measured weighted mean age for the secondary RM for that session. Common Pb correction utilized the Pb composition of the surface blank (Stern 1997). Isoplot v. 3.00 (Ludwig 2003) was used to generate concordia plots and calculate weighted means. The error ellipses on the concordia diagrams, and the weighted mean errors in the text are reported at 95% confidence unless otherwise noted. An evaluation of the long-term reproducibility of 206Pb/238U age of secondary standards indicates that the minimum precision of SHRIMP ion probe weighted mean results is $\pm 0.78\%$ (2 σ , B. Davis pers. comm). This uncertainty has been added in quadrature to the interpreted (weighted mean average) ages and is necessary when comparing results between samples analysed during separate

analytical sessions. Uncertainties reported in the Supplemental Material S3 are given at the 1σ confidence interval.

3. Thin Section Imagery

Polished thin sections were imaged using two methodologies:

3.1. Elemental Maps

Major element data and maps were acquired using a Zeiss Sigma HD Field Emission Gun analytical scanning electron microscope (ASEM) outfitted with dual 150mm2 Oxford X-MaxN silicon drift detector energy dispersive spectrometers in the School of Earth and Ocean Science, Cardiff University (UK). Element maps of 10 samples were collected using a 120 nm aperture and 20.0 kV accelerating voltage with a resulting beam current of ~4 nA. Maps were run at 95-110x magnification, with a step size of 20-22 μm, a dwell time between 3200-4000 ms and a process time of 0.5 µs. All maps were background corrected and overlaps were deconvolved using Oxford Instruments Aztec software. Chemical maps of whole thin sections of the samples were collected using a Zeiss Sigma HD field emission gun SEM installed at Cardiff University (UK). This machine is equipped with dual 150-mm2 Oxford Instruments X-MaxN energy dispersive silicon drift detectors, which enable high count rates (>1,000,000 cps) and rapid acquisition of quantitative element maps of all phases e.g. Pl anorthite and Cpx Mg#, in this case at 10 µm step ("pixel") size. The data were background-corrected using Oxford Instruments AZtec software prior to the production of element maps. Mineral major element compositions (An in Pl, Mg# in Cpx and Fo in Ol) were quantified from the element maps using the approach of (Loocke 2016). Images are reported in Supplemental Material S2.

3.2. SEM-MLA Maps

Thin section scans were created using Energy Dispersive X-ray Spectroscopy – Scanning Electron Microscopy – Mineral Liberation Analysis (SEM-MLA) and an optical microscope at Memorial University of Newfoundland (Canada). Analytical details are detailed in (Feely et al. 2019). The SEM-MLA facility in the CREAIT laboratories at Memorial University (Grant et al. 2016; Sylvester 2012) consists of a scanning electron microscope (SEM) equipped with mineral liberation analysis (MLA) software written by the University of Queensland's Julius Kruttschnitt Mineral Research Centre in Australia. The Memorial University group has developed a sophisticated, proprietary library of species identification protocols (SIPs) that can be used to indicate almost all minerals present within a sample, down to <0.3% detected unknowns using a matching threshold of 70% in the MLA software. The confidence level for the spectral match is set during the initial analysis. The software scales the probability between 0% and 100%, where 100% is a perfect match (probability of 1) and 50% is an 'average match'. New mineral spectra are added to the SIP library as they are identified. The SEM is equipped with a dual Bruker EDS detector and utilizes a field emission gun at an operating voltage of 25 kV and a beam current of 10 nA. The working distance between the sample and detector is 13.5 mm, and for the present study, the spot size was $\sim 2.5 \mu m$. The imaging scan speed was 16 microseconds, with a resolution of 500 pixels per frame (each frame 1.5×1.5 mm) and X-ray collection at 12 milliseconds. The MLA software provides a false-colour digital map of the mineral phases present within a rock thin section and it also yields mineral abundance data (as a function of the area percent of the analyzed thin section). Images are reported in Supplemental Material S2.

4. Mineral Chemistry

The mineral chemistry of olivine, orthopyroxene, clinopyroxene, plagioclase, amphibole, ilmenite, and pyrite from eleven samples (Supplemental Material S4) was analyzed using a JEOL JXA-8230 Electron Probe Microanalyzer (Trepmann) equipped with five wavelength dispersive spectrometers (WDS) at Memorial University of Newfoundland. A voltage of 15 kV and a current of 20 nA were applied for all analyses. Olivine was analyzed for Ni, Cr, Ca, Al, Si, Mg, Fe, Mn and Ti using a 3 μm beam. Pyroxene, amphibole and ilmenite were analyzed for Ni, Cr, K, Ca, Al, Si, Mg, Fe, Mn and Ti with a 1 μm beam, focusing on the cores and rims of larger grains, and the cores of smaller grains. Plagioclase was analyzed for Cr, K, Ca, Al, Si, Mg, Fe, Mn and Ti with a 1 μm beam, focusing on the cores of smaller grains. Pyrite cores and rims were analyzed for Zn, Ni, Cr, Ti, Ag, Bi, Pn, S, Si, Se, As, Cu, Co, Fe, and Mn with a 5 μm beam.

5. Whole-rock Geochemistry

All samples were prepared at the Geological Survey of Newfoundland and Labrador's Geochemistry Laboratory in St. John's, following protocols outlined by Finch et al. (2018). Major and select trace elements (Ba, Be, Cr, Sc, Zr) were determined by Inductively Coupled Plasma-Optical Emission Spectrometry (ICP-OES) following borate fusion. Volatiles were determined by loss-on-ignition (LOI) at 1000°C. Select trace elements including As, Cd, Co, Cu, Li, Ni, Pb, Rb, V and Zn, were determined by ICP-OES following 4-acid digestion. Rare-earth element (REE) and additional trace-element concentrations were determined by Inductively Coupled Plasma Mass Spectrometry (ICP-MS) or INAA (Instrumental Neutron Activation Analysis) following borate fusion. Fluoride concentrations were determined by Ion-selective Electrode. Silver (Ag) concentrations were determined by ICP-OES following digestion in nitric acid. Where an element

was analyzed using multiple methods, the value determined by the method that appears most reliable is presented (see Supplemental Material 5). Details of geochemical methods, detection limits and standard analytical errors for all techniques applied are readily available from the relevant laboratories.

6. Whole-rock Sr-Nd Isotope Analysis

Samples were analyzed at Memorial University using the procedure outlined herein. Samples are weighed into Savilex© Teflon capsules and then spiked with a mixed 150Nd/149Sm spike before being dissolved using a 6 ml (2:1) mixture of 29 M HF – 15 M HNO₃. After five days of acid digestion on a hotplate, the solution is then evaporated to dryness and taken back up in 8M HNO₃ for five days followed by 6M HCl for another five days. The sample is finally dried down and then re-dissolved in 2.5 M HCL. Samples are then loaded into a column containing cation exchange resin AG-50W-X8, H+ form, 200-400 mesh where a Sr fraction can be isolated followed by collection of bulk rare earth elements (REEs). This bulk solution is then dried and taken up in 0.18 M HCl and loaded on a second column containing Eichrom© Ln resin (50-100 mesh) to isolate Sm and Nd separately from the other REEs. Sr is purified and recuperated separately using a 1 mL column filled with Eichrom© Sr spec. resin. All reagents are purified to insure a low contamination level.

Sm and Nd concentrations and the Nd and Sr isotopic compositions are determined using a multi-collector Finnigan Mat 262 mass spectrometer in static mode for concentration determination, and dynamic mode for isotopic composition determination. Instrumental mass fractionation of Sm, Nd and Sr isotopes are corrected using a Raleigh law relative to ¹⁴⁶Nd/¹⁴⁴Nd = 0.7219, ¹⁵²Sm/¹⁴⁷Sm = 1.783 and ⁸⁸Sr/⁸⁶Sr = 8.375209. The reported ¹⁴³Nd/¹⁴⁴Nd and ⁸⁷Sr/⁸⁶Sr ratios are corrected for the deviation from repeated duplicates of standards JNdi-1 (¹⁴³Nd/¹⁴⁴Nd =

Data are reported in Supplemental Material S6.

References

- Bodorkos, S., Bowring, J.F., and Rayner, N.M. 2020. Squid3: next-generation data processing software for sensitive high-resolution ion microprobe (SHRIMP).
- Feely, M., Wilton, D.H., Costanzo, A., Kollar, A.D., Goudie, D.J., and Joyce, A. 2019. Mineral Liberation Analysis and Scanning Electron Microscopy of Connemara Marble: New Mineral Distribution Maps of an Iconic Irish Gem Material. The Journal of Gemmology, **36**: 456-466. doi:10.15506/JoG.2019.36.5.456.
- Finch, C., Roldan, R., Walsh, L., Kelly, J., and Amor, S. 2018. Analytical Methods for Chemical Analysis of Geological Materials. Government of Newfoundland and Labrador, Department of Natural Resources, Geological Survey, Open File NFLD/3316,, St. John's.
- Grant, D.C., Goudie, D.J., Shaffer, M., and Sylvester, P. 2016. A single-step trans-vertical epoxy preparation method for maximising throughput of iron-ore samples via SEM-MLA analysis. Applied Earth Science, **125**: 57-62. doi:10.1080/03717453.2015.1104056.
- Hinchey, A.M. 2010. Geology of the Northern Portion of the Silver Mountain Map area (NTS 12H/11), Southern Long Range Inlier, Newfoundland. Current Research (2010) Newfoundland and Labrador Department of Natural Resources Geological Survey, **Report 10-1**: 245-263. doi:10.13140/RG.2.2.18689.07520.
- Hinchey, A.M. 2020. Geology of the Northern Silver Mountain Map Area (NTS 12H/11). Scale 1:50 000. Newfoundland and Labrador, Department of Industry, Energy and Technology, Geological Survey, Map 2020-18, Open File, 12H/11: 1. doi:10.13140/RG.2.2.18689.07520.
- Loocke, M. 2016. The role of the axial melt lens in crustal accretion at fast-spreading mid-ocean ridges. Cardiff University.
- Ludwig, K.R. 2003. User's Manual for Isoplot 3.00 : A Geochronological Toolkit for Microsoft Excel. Berkeley Geochronology Center, Special Publication, Berkeley CA :.
- Ludwig, K.R. 2009. SQUID 2: A user's manual.
- Steiger, R.H., and Jäger, E. 1977. Subcommission on geochronology: Convention on the use of decay constants in geo- and cosmochronology. Earth and Planetary Science Letters, **36**: 359-362. doi:10.1016/0012-821X(77)90060-7.
- Stern, R.A. 1997. The GSC Sensitive High Resolution Ion Microprobe (SHRIMP): analytical techniques of zircon U-Th-Pb age determinations and performance evaluation. Radiogenic age and isotopic studies: Report 10; by Geological Survey of Canada; Geological Survey of Canada, Current Research 1997-F, .
- Stern, R.A., and Amelin, Y. 2003. Assessment of errors in SIMS zircon U–Pb geochronology using a natural zircon standard and NIST SRM 610 glass. Chemical Geology, **197**: 111-142. doi:10.1016/S0009-2541(02)00320-0.
- Sylvester, P.J. 2012. Use of the Mineral Liberation Analyzer (MLA) for mineralogical studies of sediments and sedimentary rocks. *In* Mineralogical Association of Canada Short Course. pp. 1-16.
- Tanaka, T., Togashi, S., Kamioka, H., Amakawa, H., Kagami, H., Hamamoto, T., Yuhara, M., Orihashi, Y., Yoneda, S., Shimizu, H., Kunimaru, T., Takahashi, K., Yanagi, T., Nakano, T., Fujimaki, H., Shinjo,

- R., Asahara, Y., Tanimizu, M., and Dragusanu, C. 2000. JNdi-1: a neodymium isotopic reference in consistency with LaJolla neodymium. Chemical Geology, **168**: 279-281. doi:10.1016/S0009-2541(00)00198-4.
- Trepmann, C.A. 2008. Shock effects in quartz: Compression versus shear deformation An example from the Rochechouart impact structure, France. Earth and Planetary Science Letters, **267**: 322-332. doi:10.1016/j.epsl.2007.11.035.
- Veizer, J., Ala, D., Azmy, K., Bruckschen, P., Buhl, D., Bruhn, F., Carden, G.A.F., Diener, A., Ebneth, S., Godderis, Y., Jasper, T., Korte, C., Pawellek, F., Podlaha, O.G., and Strauss, H. 1999. 87Sr/86Sr, δ13C and δ18O evolution of Phanerozoic seawater. Chemical Geology, **161**: 59-88. doi:10.1016/s0009-2541(99)00081-9.